Catalytic conversion of guaiacol to phenol and alkylphenols over Mo-promoted Ni/CeO$_2$ catalyst in supercritical ethanol

Soheil Valizadeh [a,1], Yasin Khani [a,1], Bo Sung Kang [a,1], Jinwoo Hwang [b], Jungho Jae [c], Chang Hyun Ko [d], Jeong Woo Han [e,*], Young-Kwon Park [a,*]

[a] School of Environmental Engineering, University of Seoul, Seoul 02504, South Korea
[b] Department of Chemical Engineering, Pohang University of Science and Technology (POSTECH), Pohang 37673, South Korea
[c] School of Chemical Engineering, Pusan National University, Busan 46241, South Korea
[d] School of Chemical Engineering, Chonnam National University, Gwangju 61186, South Korea
[e] Department of Materials Science and Engineering, Research Institute of Advanced Materials, Seoul National University, Seoul 08826, South Korea

A R T I C L E   I N F O

A B S T R A C T

The study explored the catalytic hydrodeoxygenation (HDO) of guaiacol using nickel-loaded cerium oxide (Ni/Ce) and molybdenum-promoted Ni/Ce (Mo-Ni/Ce) catalysts in supercritical ethanol. The use of Mo-Ni/Ce at 300 °C maximized H$_2$ production, guaiacol conversion (84.1%), and deoxygenation compared to Ni/Ce. Mo-Ni/Ce also achieved the highest efficiency for producing desired products, resulting in 7.8% phenol and 29.0% alkylphenols selectivities. Mo-Ni/Ce's better efficiency stemmed from enhanced ethanol dehydrogenation, H$_2$ dissociation and spillover, and accelerated HDO reactions owing to improved Ni dispersion and catalyst oxygen vacancies. Testing different Ni and Mo loading amounts revealed the optimum catalyst efficiency when using 20% Ni and 5% Mo (5Mo-20Ni/Ce). Temperature optimization with 5Mo-20Ni/Ce increased guaiacol conversion (up to 95.6% at 340 °C) and yielded more phenol (27.4%) and alkylphenols (66.1%). DFT calculations revealed that adding molybdena clusters notably reduced the energy required for creating oxygen vacancies, indicating enhanced catalytic properties for oxygen vacancy generation in 5Mo-20Ni/Ce.

1. Introduction

In the 21st century, humankind has faced huge challenges because of the increasing energy demand and environmental concerns related to the consumption of fossil fuels [1], necessitating the search for eco-friendly and sustainable alternative energy sources. Biomass, mainly in lignocellulosic form, is an attractive energy source for substituting fossil fuels [2,3]. Notably, lignocellulosic biomass can be chemically converted into value-added fuels using several processes, including gasification, pyrolysis, liquid-phase reforming, hydroprocessing, and oxidation [4]. However, the bio-oils produced by these processes contain very high oxygen contents and are complex mixtures of carboxylic acids, ketones, aldehydes, furans, and other compounds [5], limiting their direct application as fuel additives. Therefore, bio-oils should be upgraded to reduce their oxygen content and increase their energy value [6].

Hydrodeoxygenation (HDO), one of the most efficient technologies

for upgrading bio-oils [7], removes oxygen as H$_2$O under hydrothermally pressurized hydrogen gas (H$_2$) conditions [8]. However, the flammability of molecular hydrogen in contact with air makes it difficult to control the high H$_2$ pressure in large-scale HDO applications. Meanwhile, the high cost of H$_2$ production and compression, as well as difficulties related to H$_2$ transportation and storage, limit the implementation of HDO with the external H$_2$ supplement. Notably, replacing H$_2$ with hydrogen donor (H-donor) solvents as an alternative H$_2$ source is a highly attractive option [9]. In particular, ethanol (EtOH) has been proposed as an emerging H-donor solvent that provides active hydrogen for the HDO of bio-oil through decomposition over appropriate catalysts under supercritical conditions, allowing the deoxygenation of bio-oil to proceed without an external H$_2$ supply [10].

Importantly, phenolic compounds originating from the lignin portion of the biomass constitute a major part of the oxygenated compounds in bio-oils. Guaiacol, which simultaneously contains hydroxyl and methoxy groups, has often been chosen as a model lignin compound

* Corresponding authors.
E-mail addresses: jwhan98@snu.ac.kr (J.W. Han), catalica@uos.ac.kr (Y.-K. Park).
[1] Co-first authors

because it is the primary structure of lignin [11]. Typically, guaiacol as an intermediate compound within chemical manufacturing processes can yield a wide range of valuable end products downstream [12]. In particular, an extensive range of products has been previously reported for the catalytic HDO of guaiacol, comprising completely deoxygenated products (benzene, toluene, and cyclohexane), partially deoxygenated products (cyclohexanone, anisole, and phenol), and non-deoxygenated products (veratrole, catechol, and 6-methylguaiacol) [13,14]. Moreover, the methyl and ethyl groups evolved from EtOH can help to stabilize highly reactive phenolic intermediates by O-alkylating the hydroxyl groups and C-alkylating the aromatic rings [15], producing aromatic ethers and alkylphenols, respectively. The product distribution in the HDO process is a function of different reaction pathways, such as hydrogenation, demethylation, demethoxylation, deoxygenation, and alkylation [16]. Notably, the dominance of particular pathways in the HDO process relies on different variables, such as process parameters (e. g., temperature) and catalyst properties [17].

Nickel (Ni)-based catalysts have a strong catalytic effect on the HDO of phenolic compounds, comparable to noble metal-based catalysts [18]. Metallic Ni particles primarily facilitate the extraction of H_2 during EtOH dehydrogenation, mainly by the cleavage of C—H bonds [19]. Furthermore, metallic Ni active sites can activate hydrogen molecules by the dissociation of H_2 into hydrogen free radicals (H·) [20], which are the dominant active hydrogen species for the hydrogenolysis of C-O bonds during the HDO of phenolic compounds [21]. Moreover, Ni-based catalysts exhibit strong deoxygenation activities and weak aromatic ring saturation capacities [22]. Yoosuk et al. [23] studied the effect of Ni addition to an unsupported molybdenum sulfide catalyst on the HDO of phenol and reported enhanced hydrogen activation ability. Zuliani et al. [24] also reported a significant effect of Ni/SiO_2 catalysts on the HDO of anisole. Importantly, the efficiency of Ni-based catalysts for HDO strongly depends on the support properties, in particular its oxygen affinity [25]. Cerium oxide (CeO_2) has been suggested as a suitable support for Ni in the HDO process, mainly because of its high oxygen transfer capacity, which provides abundant oxygen vacancies (Ov) in the catalyst [26]. In the HDO process, Ov sites created on the catalyst surface can adsorb EtOH and guaiacol molecules, promoting EtOH cracking (into H_2 and alkyl groups) and guaiacol conversion [20,27]. Furthermore, the presence of Ov sites stimulates the removal of carbon deposited on the surface of metallic Ni sites [28], enhancing the catalyst stability and accelerating the HDO reactions. Schimming et al. [29] found that Ov sites on CeO_2–ZrO_2 were the main agents responsible for the enhancement of guaiacol HDO. Meanwhile, CeO_2, with outstanding thermal resistance, promotes Ni dispersions by providing a large support-metal interfacial area [30] and acting as a structural support and electron promoter, thereby improving catalytic performance [31]. Du et al. [32] observed that the interaction between Ni species and CeO_2 involved the formation of Ni-O-Ce bonds, promoting significant dispersion of Ni^0 nanoparticles.

The addition of promoters has been proposed to further enhance the activity and stability of Ni-based catalysts in HDO reactions [10]. Molybdenum (Mo) has shown excellent activity among rare earth oxides in the HDO process for guaiacol conversion. Mo can participate in hydrogenation/hydrogenolysis and subsequent demethylation reactions during HDO through its function as an acidic site [10]. Moreover, Mo active sites facilitate the polarization of EtOH molecules, serving as in situ methyl and hydrogen radicals that aid the conversion of lower alkylphenols into higher alkylphenols [33]. Cui et al. [34] reported high efficiency for partial deoxygenation and high selectivity toward alkylphenols in the HDO of guaiacol using MoO_3 in supercritical EtOH. Specifically, the addition of Mo to a Ni-based catalyst increases the number of Ov sites on the catalyst due to the various oxidation states of Mo [20] as well as enhances the metal-support interaction and Ni dispersion, which are conducive to limiting coke formation and enhancing the catalytic stability and activity [35]. The adsorption strength and orientation of guaiacol could also be altered by the

co-existence of Mo and Ni, subsequently influencing the reaction pathways [36]. Jin et al. [37] reported the high catalytic performance of Ni−Mo/CeO_2 in the H_2-free HDO of guaiacol in water as reaction media.

Despite many investigations on the catalytic HDO of guaiacol, studies on the use of Ni-based catalysts with high oxygen mobility to simultaneously extract H_2 from H-donor solvents and promote HDO reactions are limited. Accordingly, this study aimed to synthesize Ni/CeO_2 and Mo-promoted Ni/CeO_2 catalysts along with testing their activity primarily in H_2 production from supercritical EtOH and in the subsequent HDO of guaiacol to generate phenol and alkylphenols without the addition of external H_2. The effects of varied loading amounts of Ni and Mo alongside catalyst stability of Mo-Ni/CeO_2 were examined. Also, to further elucidate the reaction pathways for the production of phenol and alkylphenols, possible reaction intermediates, including catechol, phenol, and anisole, were subjected to HDO using the Mo-Ni/CeO_2 catalyst under the same conditions as those used for the HDO of guaiacol. In addition, the effects of different reaction temperatures were investigated.

2. Materials and methods

2.1. Materials

Guaiacol, a model compound for lignocellulosic biomass-derived bio-oil, was purchased from Tokyo Chemical Industry (TIC, Japan) and used in the catalytic HDO reaction. Moreover, EtOH, purchased from Duksan (Ansan, Korea), was used as the supercritical fluid to supply H_2 as well as the ethyl and methyl groups required for the deoxygenation and alkylation reactions. Cerium (IV) oxide (CeO_2), purchased from Sigma-Aldrich (USA), was used as the catalyst support. Nickel (II) nitrate hexahydrate and ammonium heptamolybdate tetrahydrate were supplied by Sigma-Aldrich (USA) and Daejung Chemical Company (Korea) and were applied as the metal and promoter for catalyst synthesis, respectively.

2.2. Catalyst preparation and characterization

In this study, two catalysts, Ni/CeO_2 and Mo-promoted Ni/CeO_2, were primarily synthesized for the EtOH conversion and HDO of guaiacol. To prepare Ni/CeO_2, an appropriate amount of Ni $(NO_3)_2 \bullet 6$ H_2O solution, as a metal precursor, was used for loading 20% Ni on the CeO_2 support via the wet impregnation method, followed by overnight drying at 120 °C, 3 h calcination at 500 °C, and 3 h reduction using 100 mL/min H_2 flow at 600 °C. In addition, Mo-promoted Ni/CeO_2 was prepared using a two-step procedure. First, modified support (5% Mo/CeO_2) was prepared using certain amounts of $(NH_4)_6Mo_7O_{24} \cdot 4$ H_2O solution and CeO_2 by the wet impregnation method, followed by overnight drying at 120 °C and 3 h calcination at 500 °C. Next, 20% Ni was loaded onto the obtained 5% Mo/CeO_2 sample using the same procedure explained for the preparation of the Ni/CeO_2 catalyst. Furthermore, to investigate the effect of different concentrations of Ni and Mo on catalyst performance, varied amounts of Ni (i.e., 15–25%) and Mo (i.e., 3–7%) were applied to prepare Mo-Ni/CeO_2 catalysts via identical procedure as explained above. Prepared catalysts were named 20Ni/Ce, 5Mo-15Ni/Ce, 5Mo-20Ni/Ce, 5Mo-25Ni/Ce, 3Mo-20Ni/Ce, and 7Mo-20Ni/Ce.

The prepared catalysts were characterized using Nitrogen adsorption-desorption, H_2-TPR, XRD, O_2-TPD, XPS, HR-TEM, and EDX spectroscopy. Detailed information regarding the catalyst characterization methods is provided in the Supplementary Material.

2.3. Testing catalytic activity

The catalytic activity was investigated in two stages using a batch-system Parr reactor (Fig. 1). First, the potential of the 20Ni/Ce and 5Mo-20Ni/Ce catalysts for the generation of H_2 from supercritical EtOH was evaluated. Briefly, 1 g of catalyst and 50 mL of EtOH were placed in
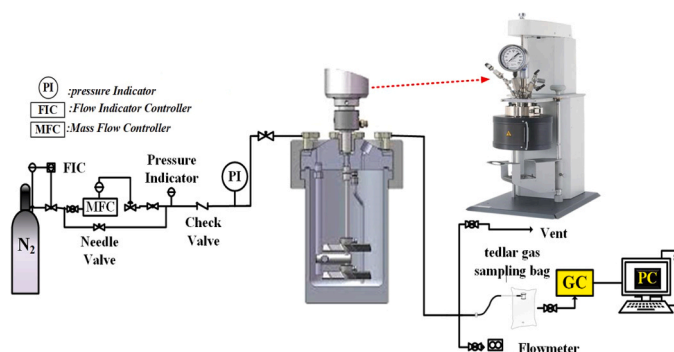
Fig. 1. Guaiacol HDO system.

a 100 mL reactor, and after the leakage test, the reactor was purged three times with N_2 to remove the remaining air. Then, the reactor containing an initial 10 bar of N_2 was heated to 300 °C and kept for 5 h with stirring at 500 rpm, creating a supercritical EtOH environment. After the reaction, the produced gas was collected at room temperature for further analysis to quantify the H_2 production. Second, the activities of the abovementioned catalysts were evaluated for the deoxygenation and production of phenol and alkylphenols in the HDO of guaiacol, where 1 g of guaiacol, 1 g of catalyst, and 50 mL EtOH were mixed, and the process was performed in the same manner as the aforementioned conditions for the first stage. After the reaction, the remaining liquid and spent catalyst were separated by filtration and collected for further chemical composition analysis of the liquid samples and coke measurement. Meanwhile, the catalyst stability of 5Mo-20Ni/Ce was evaluated by three consecutive guaiacol HDO reactions at identical

2.4. Products analysis

A GC (Agilent 7890A-USA) equipped with a thermal conductivity detector (TCD) was employed to analyze the produced gas samples. In addition, the obtained data from TCD was analyzed using Autochro 2000 (version 1.0) software. The amount of produced H_2 (mol) in each sample was quantified through the procedure given in Supplementary Material.

Furthermore, the chemical compositions of the liquid products were analyzed by GC-MS, in which the GC-7820A was coupled with an Agilent 5977E MSD. ChemStation software was used for data analysis using the National Institute of Standards and Technology (NIST) library. The internal standard method was used to quantify the initial and post-run guaiacol amounts, which was used to calculate the conversion percentage during the HDO process (Eq. 1).

$$Guaiacol \ Conversion \ (\%) = \frac{Mole \ of \ guaiacol_{initial} - Mole \ of \ guaiacol_{final}}{Mole \ of \ guaiacol_{initial}} \times 100 \qquad (1)$$

conditions.

Furthermore, the study tested the catalytic performance of 5Mo-15Ni/Ce, 5Mo-25Ni/Ce, 3Mo-20Ni/Ce, and 7Mo-20Ni/Ce in guaiacol HDO at 300 °C to examine the effect of varying Ni and Mo loading amounts. Ultimately, the activity of 5Mo-20Ni/Ce was tested in the HDO of guaiacol at different reaction temperatures (i.e., 280, 300, 320, and 340 °C) to test the effect of temperature on the product distribution.

The water content of the liquid products was measured using a Metrohm-870 KF Titrino Plus (Switzerland) device. The formed coke (wt %) was evaluated using thermogravimetric analysis (TGA), heating the used catalysts gradually from 40 °C to 900 °C in an air atmosphere (10 mL/min). The variation in weight exhibited by the catalysts was identified as coke.

2.5. Computational methods

Density functional theory (DFT) calculations were conducted to recognize the preferred sites for oxygen vacancy and assess the catalysts' capability to create an oxygen vacancy. Using DFT computations, the energy needed for producing a solitary oxygen vacancy on $CeO_2(111)$, $Ni/CeO_2(111)$, $Mo^{(IV)}$-$Ni/CeO_2(111)$, and $Mo^{(VI)}$-$Ni/CeO_2(111)$ surfaces were also calculated. All the spin-polarized DFT calculations were performed using Vienna Ab-initio Simulation Package (VASP, version 5.4.4) [38,39]. Other details regarding the DFT calculations are given in the Supplementary Material.

3. Results and discussion

3.1. Catalyst's characterization

3.1.1. Nitrogen adsorption-desorption isotherm analysis

The physical properties of all synthesized catalysts are presented in Table 1. In Mo-promoted Ni/CeO_2 catalysts, although there was a small

Table 1
Physical properties of prepared catalysts and conventional zeolites.

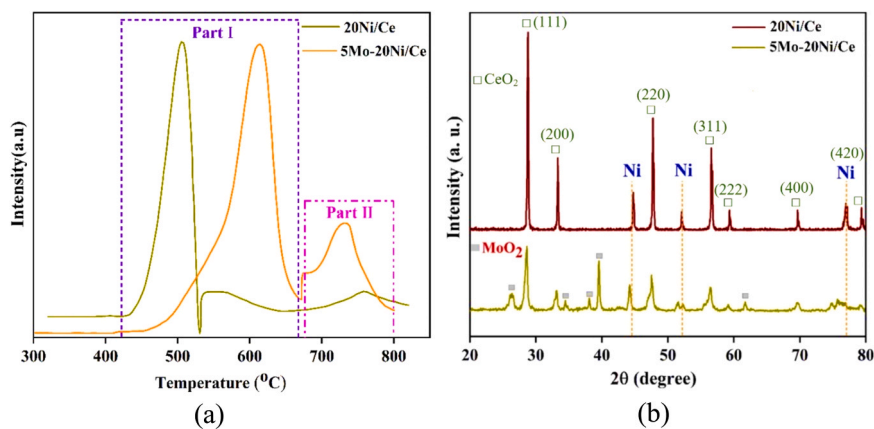| Catalyst	BET surface area (m²/g)	Total pore volume (cm³/g)	Average pore size (Å)	Ref.
20Ni/Ce	18.6	0.68	150.5	Present study
5Mo-15Ni/Ce	13.6	0.64	138.2	
5Mo-20Ni/Ce	12.9	0.62	134.3	
5Mo-25Ni/Ce	9.2	0.58	123.7	
3Mo-20Ni/Ce	13.1	0.62	136.5	
7Mo-20Ni/Ce	13.5	0.65	132.8	
HZSM-5	420	0.22	5.5	[42]
HY	735	0.42	7.4	[43]
Hbeta	650	0.35	6.9	[43]

Fig. 2. (a) H$_2$-TPR profiles of 20Ni/Ce and 5Mo-20Ni/Ce catalysts, (b) and XRD patterns of all prepared catalysts.

decrease in S$_{BET}$, total pore volume, and average pore size when raising the Ni loading from 15% to 20%, further elevating the Ni percentage to 25% greatly declined the respective values. However, increasing Mo loading from 3% to 7% resulted in negligible differences in S$_{BET}$, total pore volume, and average pore size. Even though prepared catalysts have relatively low S$_{BET}$, their higher total pore volumes and average pore sizes compared to the respective values reported for conventional catalysts such as zeolite [40], are beneficial to enhancing the efficiency of the HDO process. Greater pore volumes aid in distributing active metals effectively and enhancing their dispersion. Furthermore, larger pores facilitate easier penetration of bulkier reactants (e.g., oxygenated compounds) into the catalyst structure, ensuring better interaction with interior active sites. These attributes, minimizing mass transfer limitations, enhance catalytic activity during the HDO process [41].

3.1.2. H$_2$-TPR

Fig. 2a shows the H$_2$-TPR profiles of 20Ni/Ce and 5Mo-20Ni/Ce catalysts, where two reduction peaks were observed for both samples. In the 20Ni/Ce case, the first reduction peak started at approximately 430 °C and continued up to 530 °C, along with a weak reduction peak in the temperature range of 680 °C to 800 °C. In the 5Mo-20Ni/Ce case, two reduction peaks appeared in the temperature ranges of 460 °C to 670 °C and 680 °C to 800 °C, respectively. The first reduction peak for both catalysts (Part I) indicates the conversion of nickel oxide (NiO) particles with weak metal-support interactions into metallic Ni. However, the characteristic peaks at higher temperatures (Part II) correspond to the reduction of NiO particles, which have strong metal-support interactions. Accordingly, the reduction peak at a higher temperature in Part I and the sharper reduction peak in Part II for 5Mo-20Ni/Ce compared to those of 20Ni/Ce suggest that the addition of Mo as a

promoter enhanced the interaction between the NiO particles and CeO$_2$ (probably due to decreasing Ni particle sizes) [44], making the reduction more difficult. However, decreasing the Ni particle size and increasing the metal-support interactions can promote metal dispersion, increasing the number of active sites. Therefore, despite the more difficult reduction of 5Mo-20Ni/Ce, higher catalytic activity is expected using this catalyst than 20Ni/Ce in guaiacol HDO.

3.1.3. XRD

As shown in the XRD patterns of prepared catalysts (Fig. 2b), characteristic peaks of CeO$_2$ were detected at 2θ:28.8, 33.3, 47.8, 56.5, 59.4, 69.7, and 79.3 for both catalysts (JCPDS file No.34–0394), indicating the dominance of CeO$_2$ (111) state. Moreover, both catalysts showed Ni diffraction peaks at 2θ: 44.7, 52.1, and 77.2. In addition, diffraction peaks related to MoO$_2$ were identified in the XRD pattern of 5Mo-20Ni/Ce, suggesting that the Mo promoter was successfully doped into the crystal lattice of CeO$_2$ and placed at the grain boundaries of the Ni crystals. Notably, the 20Ni/Ce catalyst demonstrated higher Ni diffraction intensities with a smaller full width at half maximum (FWHM) than those of 5Mo-20Ni/Ce, indicating larger mean crystallite sizes for Ni. Indeed, the addition of Mo prevented the growth and agglomeration of Ni nanoparticles, leading to smaller crystal sizes and a higher dispersion of Ni over the supports. This agrees with the Ni average crystallite sizes measured from the XRD patterns using the Scherrer equation [45] for the 5Ni/Ce (29.0 nm) and 5Mo-20Ni/Ce (17.0 nm) catalysts. Therefore, the reduced Ni particle sizes in the 5Mo-20Ni/Ce catalyst reveal increased dispersion of the Ni active sites, which is expected to result in higher catalytic activity in the HDO process owing to an increase in the number of active sites. The Ni particle sizes of other Mo-promoted Ni/CeO$_2$ catalysts were also calculated based on their XRD patterns
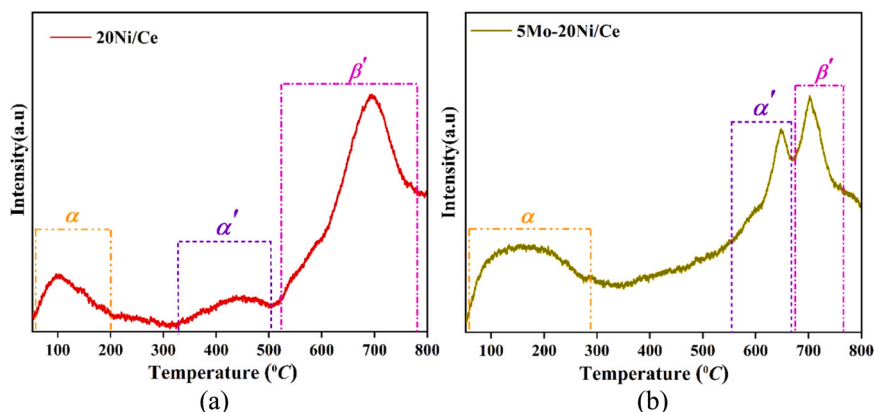

Fig. 3. O$_2$-TPD patterns of 20Ni/Ce and 5Mo-20Ni/Ce catalysts.

(Table S1), revealing the enlarging Ni average crystallite sizes with elevating Ni loading. In contrast, raising Mo loading exhibited an opposite effect on the Ni average crystallite sizes.

3.1.4. O₂-TPD

The O₂-TPD patterns of the 20Ni/Ce and 5Mo-20Ni/Ce catalysts are shown in Fig. 3, revealing three oxygen desorption peaks for each sample. The first desorption peak was observed at 105 °C and 150 °C for 20Ni/Ce and 5Mo-20Ni/Ce, respectively, relating to physically adsorbed oxygen molecules (α-oxygen species) which could not influence the catalyst's oxygen transfer capacity. The second desorption peak was detected at 450 °C and 650 °C for 20Ni/Ce and 5Mo-20Ni/Ce, respectively, corresponding to the surface monoatomic oxygen molecules adsorbed on the Ov sites (α′-oxygen species), which are mainly responsible for the oxygen mobility of the catalyst. The temperature shift might result from redox reactions on the catalyst surface, where reduction or change in oxidation states of Mo in the 5Mo-20Ni/Ce catalyst may cause a shift in the α′-oxygen peak. Finally, the third desorption peak that appeared at 700 °C for both catalysts represents the CeO₂ lattice oxygen molecules (β′-oxygen species), which could not contribute to the oxygen transfer capacity of the catalyst. Therefore, a higher intensity of α′-oxygen species peak in the 5Mo-20Ni/Ce compared to that of 20Ni/Ce reveals the enhanced generation of surface-active oxygen molecules due to the multiple oxidation states of Mo, which increases the Ov sites and improves the oxygen mobility of the catalyst. This phenomenon can facilitate the catalytic activity of 5Mo-20Ni/Ce in the HDO process and help to decrease coke formation.

3.1.5. XPS

The XPS survey spectra of 20Ni/Ce (Fig. 4a) and 5Mo-20Ni/Ce

(Fig. 4e) confirmed the presence of Ce, Ni, and O in both catalysts and proved the existence of Mo in 5Mo-20Ni/Ce. In the Ce 3d spectral regions of both catalysts (Fig. 4b,f), the peaks located at 882.6 and 889.1 were attributed to the 3d 5/2 of Ce^{3+}, while the peak at 898.4 eV represented the 3d 5/2 of Ce^{4+}. In addition, peaks associated with the 3d 3/2 of Ce^{3+} were found at binding energies of 901 and 907.5, whereas the peak at 916.8 eV corresponded to the 3d 3/2 of Ce^{4+} [46]. Therefore, the existence of Ce^{3+} and Ce^{4+} oxidation states within the CeO₂ structure due to spin binary splitting can be proven [47]. In the Ni 2p core-level spectra of the prepared catalysts (Fig. 4c,g), the peak at 852.1 eV is related to Ni 2p 3/2 of the metallic form of Ni [48]. However, two observed peaks at approximately 855.6 and 870.0 eV related to Ni 2p3/2 and Ni 2p1/2, respectively, stem from the oxide and hydroxide forms of Ni. In the core-level spectra of O 1 s in both catalysts (Fig. 4d,h), the peak areas corresponded to β′α,-·-, and α-oxygen species were observed, which can be associated with the oxygen ions of the lattice oxygen in the CeO₂ matrix, oxygen vacancies, and the surface hydroxyl (Ce–OH) group, respectively [49]. Notably, the broadened area of α′-oxygen species in the 5Mo-20Ni/Ce compared to that of 20Ni/Ce indicates the formation of more oxygen vacancies which are consistent with the results of O₂-TPD analysis. Fig. 4i exhibited the core-level spectra of Mo 3d in the 5Mo-20Ni/Ce, in which three pairs of peaks at binding energies of 228.4/231.5, 229.1/232.2, and 232.8/235.3 eV were attributed to the doublets of different oxidation states of Mo^{2+}, Mo^{4+}, and Mo^{6+}, respectively [50].

3.1.6. HR-TEM

The HR-TEM images of 20Ni/Ce (Fig. 5a) and 5Mo-20Ni/Ce (Fig. 5c) were obtained to investigate their morphological properties. The addition of Mo to 20Ni/Ce led to a sponge-like morphology and more
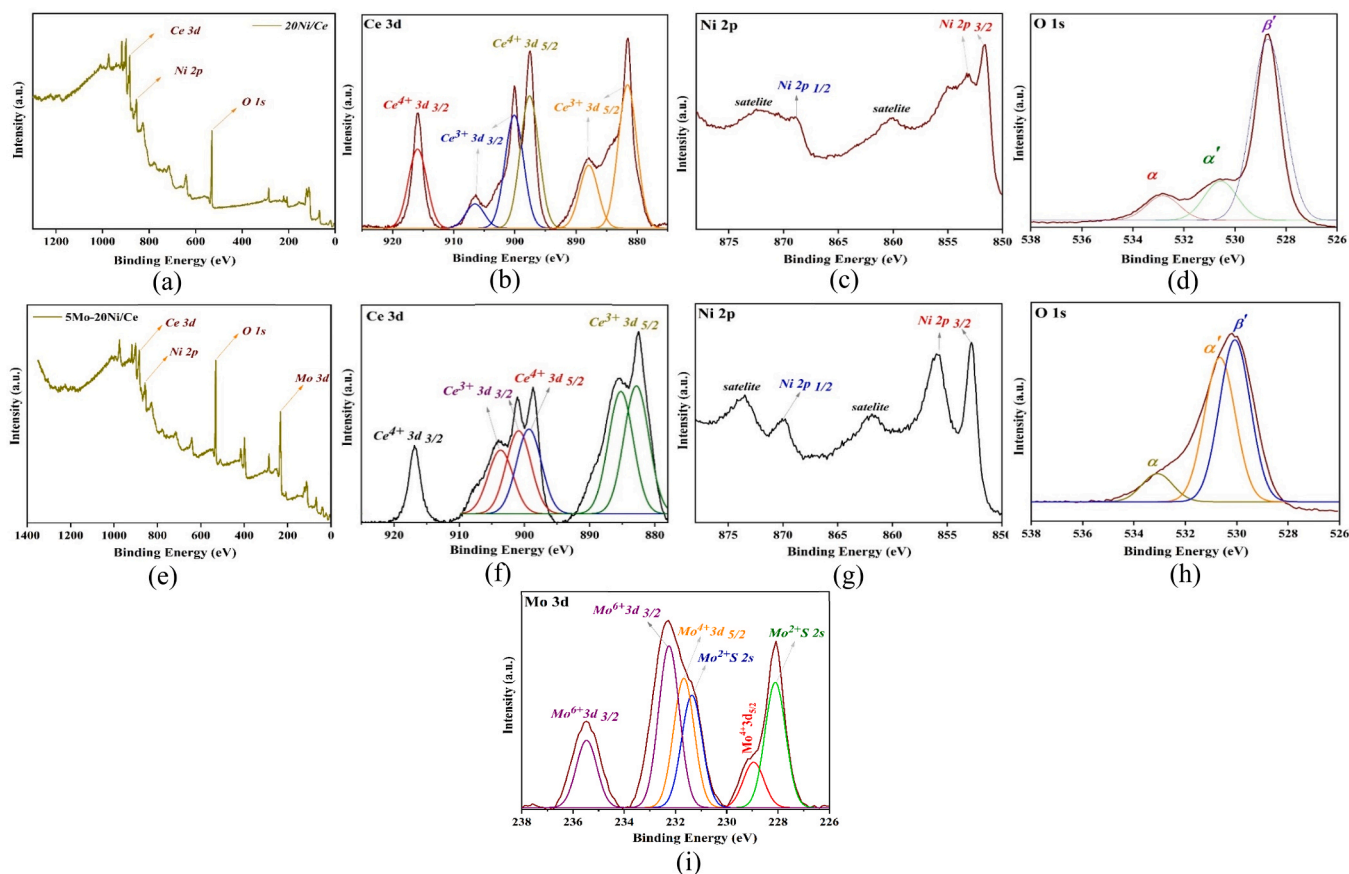

Fig. 4. XPS survey spectrum and core-level spectra of Ce 3d, Ni 2p, and O 1 s in 20Ni/Ce (a-d), and XPS survey spectrum and core-level spectra of Ce 3d, Ni 2p, O 1 s, and Mo 3d in 5Mo-20Ni/Ce (e-i).
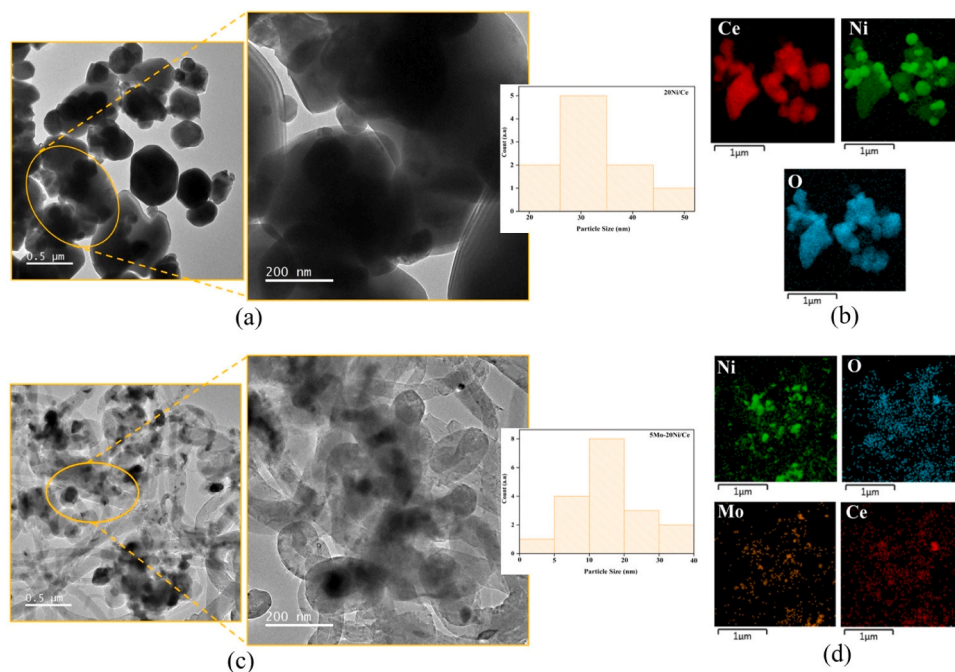
Fig. 5. HR-TEM images and EDX analysis of 20Ni/Ce (a, b) and 5Mo-20Ni/Ce (c, d) catalysts.

Table 2
Products of catalytic EtOH conversion.

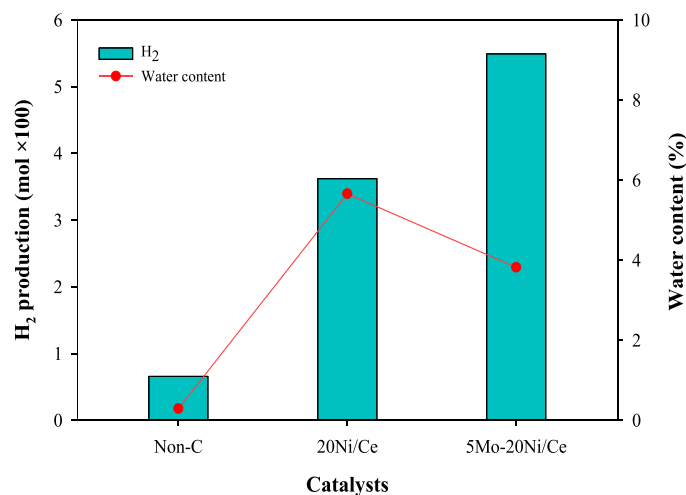| 20Ni/Ce		5Mo-20Ni/Ce	
Compounds	(PA/IS) * 100	Compounds	(PA/IS) * 100
Acetaldehyde	23.49	Acetaldehyde	38.09
1-Butanol	344.86	1-Butanol	162.30
Butanoic acid, ethyl ester	5.16	Butanoic acid, ethyl ester	37.28
1-Hexanol	18.18	Hexanoic acid, ethyl ester	10.85
Butane, 1-(1-ethoxyethoxy)-	6.43	Ethane, 1,1-diethoxy-	24.05
Hexanoic acid, ethyl ester	2.53	Butane, 1,1-diethoxy-	6.77
		Butane, 1-(1-ethoxyethoxy)-	4.33

*PA: peak area *IS: Internal Standard

homogeneity of Ni particles, which were conducive to providing better surface contact between the Ni active sites and reactants. Moreover, the reduced particle size distribution and enhanced dispersion of Ni particles due to Mo addition were evident, attributed to the role of Mo in controlling Ni particle grain growth. In addition, the EDX analysis (Fig. 5b,d) confirmed the presence of the constituent elements of 20Ni/Ce and 5Mo-20Ni/Ce. Meanwhile, the elemental mapping images show a more homogeneous and better dispersion of Ni particles in the 5Mo-20Ni/Ce compared to Ni/Ce. The improved distribution of Ce particles in the 5Mo-20Ni/Ce than 20Ni/Ce, shown in elemental mapping images, is ascribed to Mo's influence on altering the surface charge of the catalyst, which creates electrostatic repulsion between particles, preventing their aggregation [51]. Overall, the sponge-like morphology, smaller particle sizes, higher dispersion, and greater homogeneity of Ni particles on 5Mo-20Ni/Ce than on 20Ni/Ce, which are consistent with the results of H_2-TPR and XRD analyses, could positively influence the catalyst efficiency in the HDO process.

3.2. H_2 generation ability of prepared catalysts

The catalytic potential of 20Ni/Ce and 5Mo-20Ni/Ce for H_2 production from supercritical EtOH at 300 °C was evaluated. The liquid samples provided by EtOH cracking over both catalysts (Table 2) mainly comprised 1-butanol along with small amounts of other alcohols, aldehydes, ethers, and esters, which was consistent with the products reported from the catalytic cracking of EtOH at 300 °C using Mo-Ni/activated carbon [44]. Moreover, the percentage of water in the liquid phase was measured (Fig. 6), showing 0.29%, 5.66%, and 3.82% water content produced from EtOH cracking in non-catalytic test and using 20Ni/Ce and 5Mo-20Ni/Ce catalysts, respectively.

The gas samples were collected and analyzed after the reaction (Fig. 6), revealing that the relative content of produced H_2 (mol × 100) by EtOH cracking significantly enhanced from 0.66 in the non-catalytic test to 3.62 using 20Ni/Ce catalyst. Furthermore, the addition of Mo to Ni/Ce as a promotor enhanced the production of H_2 to 5.49. In addition to H_2, CH_4 and CO, together with a small amount of CO_2, were produced over both catalysts. Similarly, the enhanced generation of H_2 due to adding Mo to Ni-based catalysts has been previously reported [44].
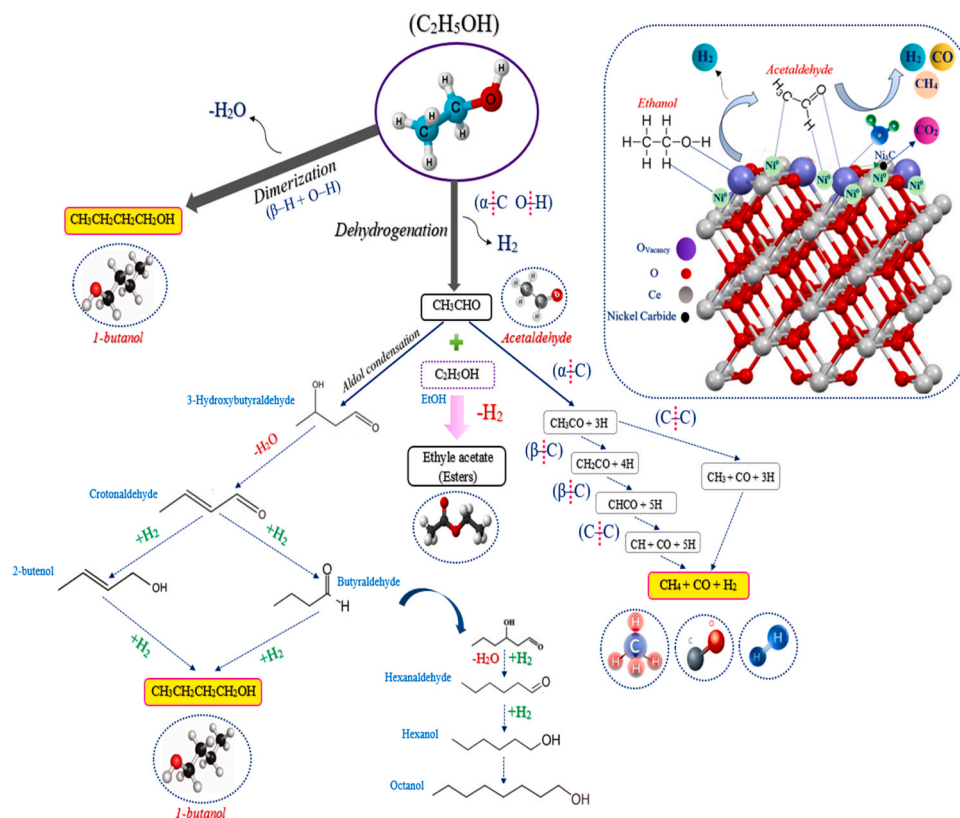

Fig. 6. Hydrogen generation from EtOH cracking.

Fig. 7. Suggested pathways for catalytic cracking of EtOH in a supercritical condition.

3.2.1. Possible pathways of EtOH cracking

Based on the chemical composition and water content of the liquid phase and the generation of H_2 in the gaseous phase, two possible reaction pathways are suggested for EtOH cracking over the employed catalysts (Fig. 7). First, direct dimerization of EtOH most likely happens via self-condensation of two EtOH molecules, in which β—H group in one molecule bonds with the O—H group in another EtOH molecule, producing 1-butanol along with releasing H_2O as a by-product [52]. Second, EtOH probably undergoes dehydrogenation via the cleavage of α—C and O—H bonds to produce acetaldehyde by releasing H_2 [53], followed by three possible sub-pathways. In the initial sub-pathway, aldol condensation of acetaldehyde forms 3-hydroxybutyraldehyde, which undergoes consecutive dehydration and hydrogenation reactions to form 1-butanol [54,55]. However, aldol condensation is kinetically and thermodynamically limited compared to the self-condensation route. As no intermediates in the aldol condensation pathway were detected, it is suggested that 1-butanol was mainly produced by direct EtOH dimerization in this study. Moreover, ethyl acetate can be formed by the reaction of acetaldehyde with EtOH molecules, further releasing H_2 [56]. Most importantly, acetaldehyde can be consecutively decomposed via cleavage of the α—C, β—C, and C—C bonds to produce different gaseous products (H_2, CH_4, and CO) [57,58].

Accordingly, the higher 1-butanol and water contents produced using 20Ni/Ce compared to those obtained using 5Mo-20Ni/Ce revealed that the direct dimerization pathway in EtOH cracking occurred to a greater extent exceeding this catalyst. However, the higher H_2 production over 5Mo-20Ni/Ce indicated that this catalyst stimulated the dehydrogenation pathway more effectively than 20Ni/Ce. The higher production of esters using 5Mo-20Ni/Ce is also consistent with these explanations.

Notably, the competitive catalytic function of C—O, C—C, C—H, and O—H bonds over a catalyst surface determines the dominant reaction pathway and product distribution of EtOH cracking [57]. The proposed catalytic function of 20Ni/Ce in the EtOH cracking process (Fig. 7)

demonstrates the dual functionality of the metallic Ni and Ov sites on the catalyst for H_2 generation. The metallic Ni sites on the catalyst can adsorb EtOH and rupture its C—H and C—C bonds, which are crucial for the dehydrogenation pathway, and participate in H_2 generation [19]. Moreover, the redox cycle of Ce ($Ce^{4+} \leftrightarrow Ce^{3+}$) during the HDO reaction creates oxygen-deficient conditions on the catalyst surface. It enhances the oxygen transfer capacity, which is conducive to the cleavage of the O—H bond of EtOH and further stimulates the dehydrogenation pathway [59,60]. Meanwhile, the water resulting from EtOH cracking can be further adsorbed on the Ov sites of the catalyst, facilitating the conversion of acetaldehyde into gaseous products (e.g., H_2).

Consequently, 5Mo-20Ni/Ce showed higher activity for H_2 generation than 20Ni/Ce because of the more effective stimulation of the dehydrogenation pathway and the subsequent cracking of acetaldehyde into gaseous compounds. These phenomena can primarily be attributed to the smaller size and enhanced dispersion of metallic Ni particles owing to Mo addition, consistent with the results of XRD, H_2-TPR, and HR-TEM analyses, which increased the accessibility of EtOH to the metal-support interfacial sites [61]. Moreover, the enhanced oxygen mobility of the catalyst as a result of Mo incorporation, as confirmed by the results of O_2-TPD and XPS analyses, was another reason for the higher potential of 5Mo-20Ni/Ce for H_2 generation.
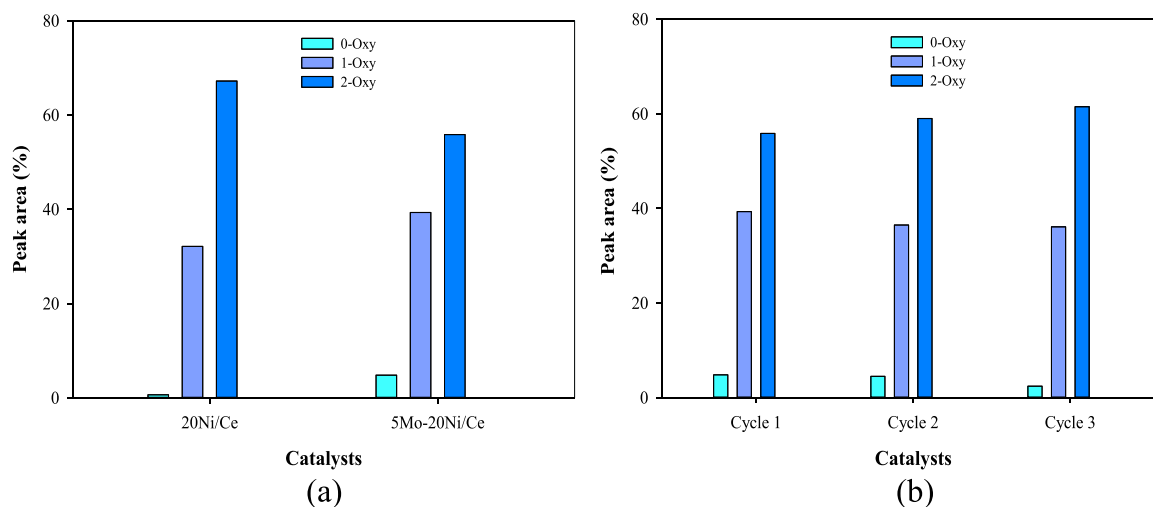
3.3. Catalytic HDO of guaiacol

3.3.1. Comparison of 20Ni/Ce and 5Mo-20Ni/Ce

The efficiency of the prepared catalysts in the deoxygenation and generation of phenol and alkylphenols in the HDO of guaiacol at 300 °C was investigated. The guaiacol conversions were obtained at 72.5% and 84.1% using 20Ni/Ce and 5Mo-20Ni/Ce, respectively (Table 3). Moreover, the investigation of the guaiacol conversion products indicated that the higher content of 0- and 1-oxy compounds, while a lower content of 2-oxy compounds, were produced using 5Mo-20Ni/Ce than those obtained using 20Ni/Ce (Fig. 8a). The higher H_2 generation ability of

Table 3

Distribution of different products (peak area %) from HDO of guaiacol in supercritical EtOH.

Catalyst	Guaiacol conversion (%)	Methoxy benzenes	Alk-methoxy phenols	Aromatic ethers	Phenol	Lower alkylphenols		Higher alkylphenols	Hydrocarbons	Coke yield (wt%)
						C7-C8	C9-C10	C11-C16		
20Ni/Ce (300 °C)	72.5	1.9	66.9	-	20.6	4.8	5.1	-	0.7	1.22
5Mo-20Ni/Ce (300 °C) Cycle 1	84.1	8.5	42.1	7.8	7.8	6.6	14.3	8.1	4.8	0.45
5Mo-20Ni/Ce (300 °C) Cycle 2	83.0	16.0	41.1	1.9	6.9	8.5	10.5	10.6	4.5	-
5Mo-20Ni/Ce (300 °C) Cycle 3	81.5	14.4	44.3	2.8	4.5	11.9	15.4	4.3	2.4	-
5Mo-15Ni/Ce (300 °C)	78.2	16.9	41.3	9.7	3.6	11.4	14.1	0.8	2.2	0.55
5Mo-25Ni/Ce (300 °C)	89.1	1.7	64.7	6.8	4.5	10.3	11.0	1.0	-	1.02
3Mo-20Ni/Ce (300 °C)	76.0	13.5	33.2	15.7	6.5	12.2	13.8	2.4	2.7	0.96
7Mo-20Ni/Ce (300 °C)	71.5	7.5	52.6	5.1	8.3	12.3	11.0	3.2	-	0.40
5Mo-20Ni/Ce (280 °C)	76.9	17.7	55.1	9.6	-	3.0	5.1	8.0	1.5	-
5Mo-20Ni/Ce (300 °C)	84.1	8.5	42.1	7.8	7.8	6.6	14.3	8.1	4.8	-
5Mo-20Ni/Ce (320 °C)	89.2	9.5	31.9	9.0	9.2	8.3	16.3	14.1	1.7	-
5Mo-20Ni/Ce (340 °C)	95.6	3.1	1.00	2.5	27.4	52.2	12.8	1.0	-	-

Fig. 8. Distribution of guaiacol HDO products based on the oxygen number: (a) Using different catalysts at 300 °C, and (b) Using 5Mo-20Ni/Ce in three consecutive cycles at 300 °C.

5Mo-20Ni/Ce was probably responsible for the greater extent of deoxygenation during guaiacol HDO. However, the low amount of fully deoxygenated (0-oxy) products suggests that the H_2 supplied for the hydrogenation reactions was insufficient, revealing the occurrence of partial deoxygenation during the catalytic guaiacol HDO in this study.

The distribution of the different products (peak area %) from guaiacol HDO (Table 3) showed that alkylated (Alk)-methoxyphenols, mainly 4-ethylguaiacol, comprised a major part of the products. In particular, the higher selectivity for Alk-methoxyphenols was obtained using 20Ni/Ce (66.9%) compared to that produced using 5Mo-20Ni/Ce (42.1%). Most importantly, the selectivities for phenol and alkylphenols were obtained at 20.6% and 9.9%, respectively, using 20Ni/Ce, and 7.8% and 29.0%, respectively, using 5Mo-20Ni/Ce. Thus, the enhanced selectivity toward alkylphenols at the expense of Alk-methoxyphenols and phenol reveals the enhancement of consecutive deoxygenation and alkylation reactions employing 5Mo-20Ni/Ce.

The alkylphenols produced in this study were classified based on the carbon number into lower alkylphenols (C7-C10) and higher alkylphenols (C11-C16). Lower alkylphenols mainly consisted of methylphenols and ethylphenols, while higher alkylphenols predominantly contained compounds with isopropyl and tert-butyl groups attached to the phenol's ring. The alkylphenols generated over 20Ni/Ce contained only lower alkylphenols (C7-C10). However, using 5Mo-20Ni/Ce, different types of lower and higher alkylphenols, such as 3-methylphenol, 3,4-dimethylphenol, 3-ethylphenol, 2,5-diethylphenol, 5-isopropyl-2-methylphenol, 2,4-diisopropylphenol, and 2,6-diisopropylphenol were generated, confirming the promotion of deoxygenation and alkylation reactions.

Moreover, small amounts of methoxybenzenes (e.g., veratrole and 4-methylveratrole) and hydrocarbons (e.g., 3-methylphenanthrene and trans-2-Pentene) were identified in the guaiacol HDO products using both tested catalysts. In contrast, aromatic ethers, such as 2-
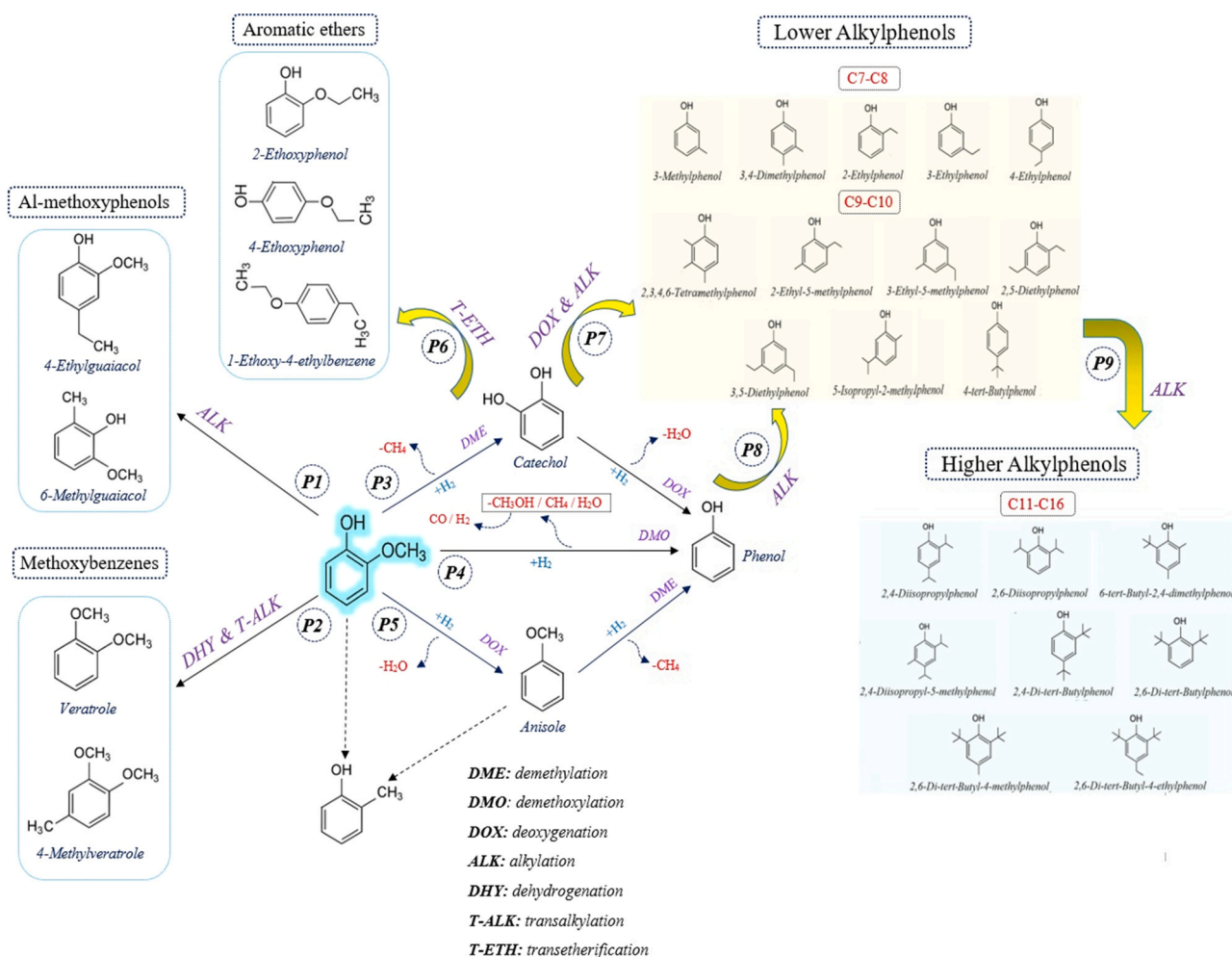
Fig. 9. Tentative possible pathways for guaiacol HDO in supercritical EtOH.

ethoxyphenol and 1-ethoxy-4-ethylbenzene, were generated only over 5Mo-20Ni/Ce. Similar product distribution was reported from the HDO of guaiacol under 340 °C for 4 h using a molybdenum carbide catalyst [62].

The quantity of coke deposited on the catalysts was evaluated (Table 3), revealing coke yields of 1.22 wt% for 20Ni/Ce and 0.45 wt% for 5Mo-20Ni/Ce. The reduced coke yield on 5Mo-20Ni/Ce is linked to Mo's dual effects on improving Ni dispersion and enhancing the catalyst's oxygen mobility characteristics.

3.3.1.1. Tentative possible pathways of guaiacol HDO. Deoxygenation, demethoxylation, demethylation, and alkylation are the main reactions involved in the HDO of guaiacol [63,64]. Fig. 9 shows the possible tentative pathways and intermediates suggested for the catalytic HDO of guaiacol in this study.

Alk-methoxyphenols, the major products, are formed by substituting methyl or ethyl groups, originating from EtOH cracking, into the benzene ring of guaiacol, called alkylation (pathway 1). For instance, 4-ethylguaiacol is produced by adding an ethyl group to the guaiacol molecules. Moreover, methoxybenzenes are produced by consecutive dehydrogenation (H^+ removal) and intermolecular transalkylation of guaiacol molecules (pathway 2) [34]. For example, veratrole, as an early reaction intermediate of the guaiacol HDO is generated by the substitution of H^+ in the hydroxyl group of guaiacol with a methyl radical ($H_3C\cdot$), derived from guaiacol cleavage or EtOH cracking [65]. Furthermore, 4-methylveratrole is generated by the reaction of $H_3C\cdot$ with the benzene ring at the ortho-position of veratrole.

In addition, three possible pathways have been suggested for the conversion of guaiacol to phenol: demethylation/deoxygenation, direct demethoxylation, and deoxygenation/demethylation. In demethylation/deoxygenation (pathway 3), the hydrogenolysis of the ArO−CH$_3$ bond in guaiacol primarily generates catechol with the release of CH$_4$ [66]. Subsequently, one of the hydroxyl groups in catechol further adsorbs hydrogen radicals (H·) originating from gaseous hydrogen and is eliminated as a form of H_2O by deoxygenation reaction, transforming catechol into phenol [67]. In direct demethoxylation (pathway 4), phenol is directly produced by hydrogenating the Ar−OCH$_3$ bond and removing the OCH$_3$ group from guaiacol, producing methanol as a by-product [64]. During deoxygenation/demethylation (pathway 5), anisole is initially generated because of the removal of the hydroxyl group from guaiacol by the activation of the Ar−OH bond [68], which then undergoes demethylation to produce phenol [69]. Hydrocarbons are produced when phenol undergoes a series of reactions, including deoxygenation and hydrogenation.

In addition to the conversion of catechol to phenol, catechol also undergoes two other pathways. Aromatic ethers can be generated by the transetherification of catechol (pathway 6) [70], and catechol can be converted into lower alkylphenols via consecutive deoxygenation and alkylation reactions (pathway 7). Moreover, phenol can be subjected to alkylation to produce lower alkylphenols (pathway 8). Ultimately, higher alkylphenols can be formed via a reaction pathway, in which the H atom at the −C of the lower alkylphenols is consecutively replaced with methyl or ethyl groups provided by the EtOH medium (pathway 9) [34].

The occurrence and rate of different pathways for the transformation of guaiacol to phenol and alkylphenols mainly depend on the catalytic performance for the activation and rupture of various C–O linkages in the molecular structure of guaiacol. The energy sequence of these bonds is as follows: phenolic hydroxyl group (Ar–OH, 414 kJ.mol^{-1}) > methoxy group (Ar–OCH$_3$, 356 kJ.mol^{-1}) > methyl group (ArO–CH$_3$, 247 kJ.mol^{-1}) [71]. Accordingly, proceeding the guaiacol HDO toward pathway 3 is the most favorable route as ArO–CH$_3$ linkage has the lowest dissociation bond energy, resulting in the production of a large quantity of catechol which can then be simply converted to phenol and alkylphenols completely owing to the high reactivity [7]. In addition, the direct transformation of guaiacol to phenol (pathway 4) is expected to occur to some extent. On the contrary, the probability of the occurrence of pathway 5 is low as the hydrogenolysis of Ar–OH linkage is thermodynamically less favorable [72].

To further elucidate the reaction pathways for the production of phenol and alkylphenols, possible reaction intermediates, including catechol, phenol, and anisole, were subjected to HDO using the 5Mo-20Ni/Ce catalyst under the same conditions as those used for the HDO of guaiacol. HDO of anisole with a 15.4% conversion did not produce any alkylphenols. Considering the low reactivity of anisole and the lack of this compound in the products of guaiacol HDO, pathway 5 was completely excluded from this study. Phenol, with a 27.9% conversion, was mainly converted to C7-C8 (73.2%) and C9-C10 (18.6%) alkylphenols. In the case of catechol, 97.6% conversion was obtained with the production of phenol (3.1%), as well as C7-C8 (5.2%), C9-C10 (14.0%), and C11-C16 (9.0%) alkylphenols, revealing that product distribution was more comparable with that obtained in the HDO of

guaiacol using 5Mo-20Ni/Ce (Table 3). Consequently, it can be speculated that demethylation/deoxygenation (pathway 3) was the dominant pathway for the production of phenol and alkylphenols from the HDO of guaiacol in this study, producing catechol as an intermediate, followed by the production of phenol and alkylphenols through a series of deoxygenation and alkylation reactions. In addition, the direct transformation of guaiacol to phenol (pathway 4) probably occurred to some extent, although it cannot be considered a competitive route for guaiacol conversion in this study. The presence of a considerable amount of CH$_4$ in the gaseous phase and the detection of a small amount of methanol in the post-run liquid samples are consistent with the aforementioned explanations. Similarly, previous studies have reported catechol as the main intermediate in guaiacol conversion in supercritical EtOH [73,74].

3.3.1.2. Possible Pathways toward phenol and alkylphenols over 5Mo-20Ni/Ce. The catalytic functional mechanism of 5Mo-20Ni/Ce for the conversion of guaiacol to phenol and alkylphenols is shown in Fig. 10. As shown in Fig. 10a, guaiacol was first adsorbed on the catalyst surface by bonding its methoxy group (–OCH$_3$) to Mo- or support (CeO$_2$)- related Ov sites. Subsequently, the weakened C–O bond of the methoxy group (–OCH$_3$) linked to the Ov sites was primarily ruptured, releasing a methyl radical (H$_3$C$\cdot$) and an intermediate agent [20], which then adsorbed one of the hydrogen radicals (H$\cdot$) due to high proton affinity, converting to CH$_4$ and catechol, respectively [75]. Notably, metallic Ni sites are responsible for H$_2$ dissociation into hydrogen radicals and the migration of hydrogen spillover to the Ov sites during the HDO reaction [76].

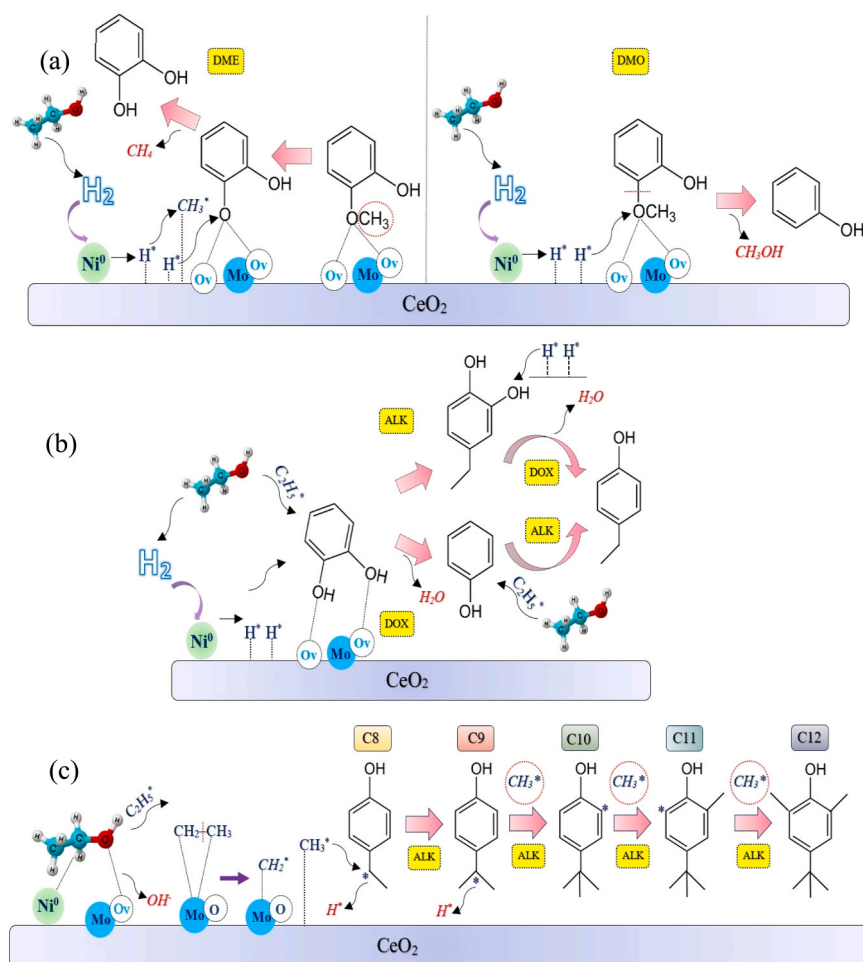Furthermore, the generation of C7-C8 alkylphenols from catechol

Fig. 10. Catalytic functions of 5Mo-20Ni/Ce in the HDO of guaiacol.

intermediate over 5Mo-20Ni/Ce was based on the interaction of two adjacent hydroxyl groups and Ov sites on the catalyst surface, as indicated in Fig. 10b. The hydroxyl group (—OH) of catechol bonds to the Ov sites, which then proceeds via two possible routes. Catechol undergoes dehydration, in which —OH is eliminated owing to the angle strain effect resulting in phenol formation as an intermediate. In contrast, the linkage of catechol with ethyl group (−CH₂CH₃) originating from EtOH cracking can form 3-methylcatechol as another possible intermediate. Subsequently, the two intermediates (phenol and 3-methylcatechol) were subjected to alkylation and deoxygenation, respectively, producing C7-C8 alkylphenols. Because of the lack of 3-methylcatechol in the HDO products of guaiacol over 5Mo-20Ni/Ce, it is difficult to assume that it is an intermediate in the production of C7-C8 alkylphenols. Therefore, it is suggested that guaiacol was initially transformed into catechol and phenol via pathway 3, followed by the alkylation of phenol to lower alkylphenols (pathway 8). Notably, the increase in alkylphenols at the expense of phenol in the case of 5Mo-20Ni/Ce compared with those produced over 20Ni/Ce is consistent with the aforementioned explanations.

Furthermore, considering the absence of isopropyl-and butyl (tert-, sec-)-derived aliphatic compounds in the liquid products of guaiacol HDO, the direct substitution of isopropyl and butyl groups or isomerization with interrelated alkylphenols did not occur in the generation of higher alkylphenols. Thus, it is postulated that the lower alkylphenols are more likely precursors of higher alkylphenols through their consecutive substitution with methyl or ethyl groups (alkylation) provided by the EtOH medium (Fig. 10c). For example, the C atom placed on the benzene ring of ethylphenols, with electrons in sp² hybridized orbits, has a strong attraction effect on electrons in sp³ hybridized orbits of –C in the ethyl group, attracting the adjacent hydrogen electron and activating the H atom [34]. Ethylphenols then might lose the activated hydrogen (H·) from —C on its ethyl group and instead capture the available methyl group supplied from cleavage of EtOH-derived ethyl group, increasing carbon number and successive transformation of lower alkylphenols to higher alkylphenols [74]. A similar reaction pathway was suggested for the generation of higher alkylphenols in the catalytic HDO of guaiacol over Re₂O₇ in supercritical EtOH [74].

The methyl group can be created by the demethylation of guaiacol or EtOH. However, because the alkylphenol products from catechol were similar to those produced from guaiacol, it can be concluded that the methyl groups were mostly derived from supercritical EtOH and not from guaiacol. Initially, the elimination of the —OH group from the EtOH molecules owing to bonding on the Ov sites of the catalyst generated abundant ethyl groups [27]. Meanwhile, some ethyl groups were possibly created via the cleavage of EtOH over the metallic Ni sites. Subsequently, when adsorbed to the Mo oxygen vacancies, ethyl groups may form metallacycles with Mo with the help of a high oxygen concentration by capturing the surplus of free electrons on the Mo surface. Subsequently, the metallacycles ruptured, creating methyl groups on the Mo atoms [44].
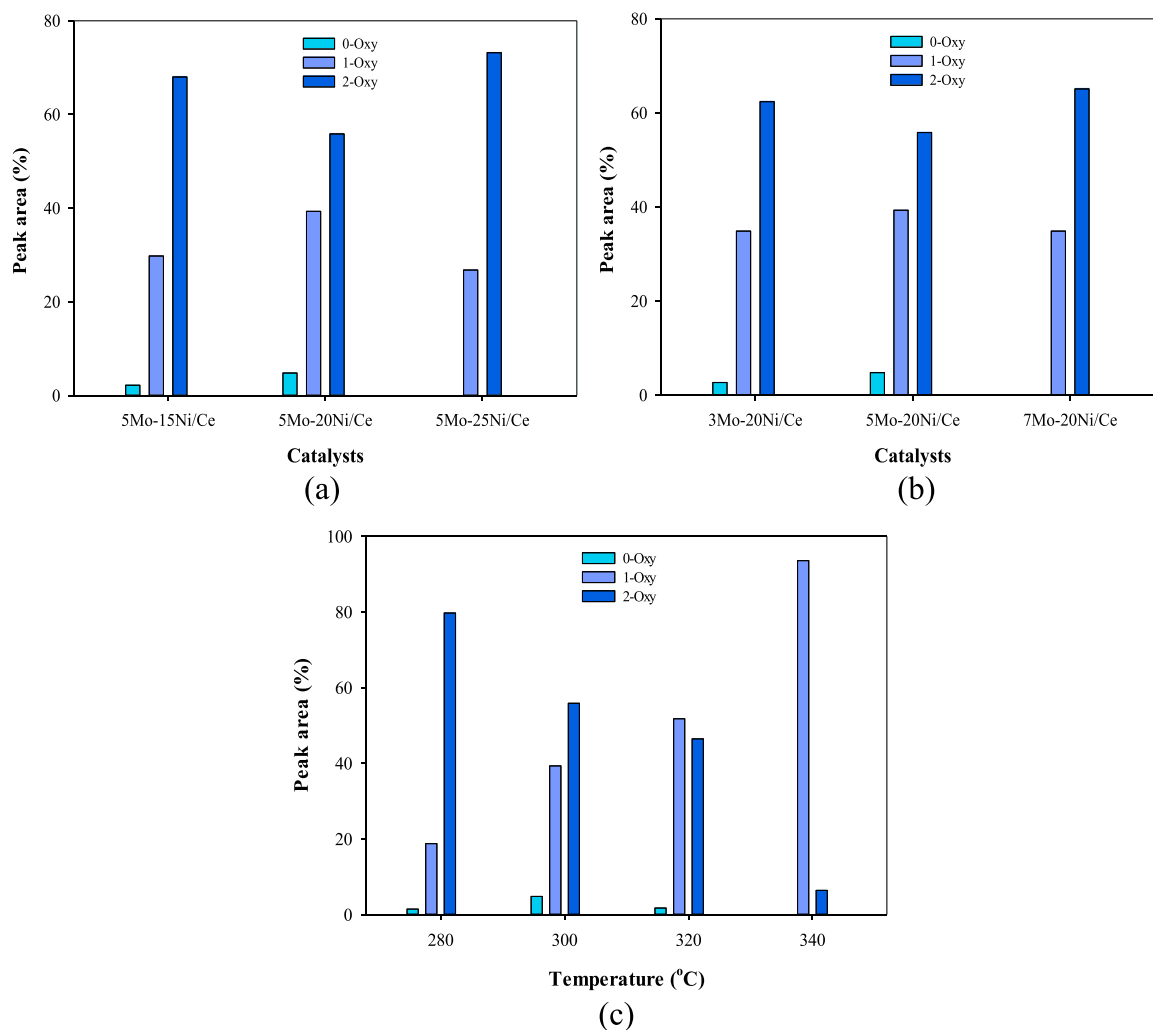

Fig. 11. Distribution of guaiacol HDO products based on the oxygen number using Mo-promoted Ni/CeO₂ catalysts with varied Ni and Mo percentages at 300 °C (a-b), and using 5Mo-20Ni/Ce at different reaction temperatures.

Overall, the better catalytic performance of 5Mo-20Ni/Ce than that of 20Ni/Ce can be ascribed to the promoted EtOH dehydrogenation, H_2 dissociation, and hydrogen radical spillover, along with the enhanced demethylation, deoxygenation, and alkylation reactions due to the dual functionality of the smaller and well-dispersed metallic Ni particles and the higher oxygen mobility properties of the catalyst [77].

3.3.2. Testing the catalytic stability of 5Mo-20Ni/Ce

To examine the catalytic stability of 5Mo-20Ni/Ce for the deoxygenation and production of phenol and alkylphenols, the HDO of guaiacol at 300 °C was carried out in three consecutive cycles. The guaiacol conversions were obtained at 84.1%, 83.0%, and 81.5% in three runs (Table 3). As indicated in Fig. 8b, the proportions of 0-oxy and 1-oxy compounds experienced a slight reduction, ranging from 4.5% and 39.3%, respectively, in the 1st run to 2.4% and 36.1%, in the 3rd run, while 2-oxy compounds marginally increased from 55.9% to 61.5% in three consecutive tests. As presented in Table 3, the distributions of different products from all three runs were comparable. In particular, the selectivities towards phenol and alkylphenols were obtained at 7.8% and 29%, respectively, in the 1st cycle, 6.9% and 29.6% in the 2nd cycle, and 4.5% and 31.7% in the 3rd cycle. Nonetheless, it can be observed that the capability of the catalyst for the transformation of lower alkylphenols to higher alkylphenols was decreased in the 3rd test.

Overall, the aforementioned results exhibit that 5Mo-20Ni/Ce substantially maintained its catalytic efficacy for extracting H_2 from EtOH cracking, supplementing hydrogen radicals, and facilitating demethylation, deoxygenation, and alkylation reactions. This aligns with a negligible coke deposited over the catalyst surface during guaiacol HDO (Table 3), corroborating the significance of small and well-dispersed Ni particles and the high potential of oxygen vacancy formation in the 5Mo-20Ni/Ce catalyst.

3.3.3. Effect of different Ni loading amounts

To explore the effect of varied Ni loading amounts on the deoxygenation and the production of desired products (i.e., phenol and alkylphenols), the activities of 5Mo-15Ni/Ce, 5Mo-20Ni/Ce, and 5Mo-25Ni/Ce catalysts were investigated in the guaiacol HDO at 300 °C. The conversion of guaiacol increased by augmenting the Ni loading on the catalyst from 15% (78.2%) to 25% (89.1%) (Table 3). However, although the deoxygenation capability was enhanced by elevating the Ni percentage from 15% to 20%, leading to augmented 0-oxy and 1-oxy compounds at the expense of 2-oxy compounds, further enhancement of Ni loading to 25% dramatically decreased the deoxygenation potential of the 5Mo-25Ni/Ce catalyst (Fig. 11a). Likewise, a similar trend was also observed in the selectivities of phenol and alkylphenols over three tested catalysts (Table 3). The selectivities of phenol and alkylphenols were acquired at 3.6% and 26.3%, respectively, using 5Mo-15Ni/Ce, 7.8% and 29.0% using 5Mo-20Ni/Ce, and 4.5% and 22.3% using 5Mo-25Ni/Ce. Notably, the optimum catalytic efficiency for the conversion of lower alkylphenols to higher alkylphenols was obtained using 5Mo-20Ni/Ce. Moreover, the analysis of coke yield demonstrated a significant increase in coke deposition over 5Mo-25Ni/Ce compared with 5Mo-15Ni/Ce and 5Mo-20Ni/Ce, which matches the catalytic performance of these catalysts.

These results could be attributed to the physical properties, crystallinity, and Ni particle sizes in the three examined catalysts. Even though the increase of Ni loading from 15% to 20% enhanced the number of catalyst active sites, it seems that the excessive Ni loading (25%) led to partial agglomeration of Ni particles. This phenomenon not only blocked some pore entrances in the CeO_2 structure, in agreement with nitrogen adsorption-desorption isotherm analysis (Table 1) but also decreased the crystallinity of the catalyst by increasing the Ni particle sizes, which is consistent with calculated Ni average crystallite sizes (Table S1). Consequently, 5Mo-20Ni/Ce with an appropriate amount of well-dispersed and small Ni active sites more effectively promoted the HDO of guaiacol toward the generation of phenol and alkylphenols.

3.3.4. Effect of different Mo loading amounts

The performances of 3Mo-20Ni/Ce, 5Mo-20Ni/Ce, and 7Mo-20Ni/Ce catalysts were evaluated in the guaiacol HDO at 300 °C to investigate the effect of varied percentages of Mo as a promoter on the deoxygenation and the generation of desired products (i.e., phenol and alkylphenols). The guaiacol conversion was enhanced by increasing the Mo loading from 3% (76.0%) to 5% (84.1%), however, it was plunged to 71.5% by a further increase of Mo to 7% (Table 3). Furthermore, an identical trend was observed in the deoxygenation activity of catalysts (Fig. 11b), wherein the maximum 0-oxy and 1-oxy compounds while minimum 2-oxy compounds were obtained using 5Mo-20Ni/Ce. Moreover, while the amounts of yielded phenol were comparable across the three catalysts, various alkylphenols showed distinct distributions (Table 3). The use of 3Mo-20Ni/Ce exhibited a higher selectivity toward C7-C8 alkylphenols, whereas the employment of 5Mo-20Ni/Ce augmented the selectivities of C9-C10 and particularly C11-C16 alkylphenols. This can be ascribed to the role of Mo active sites on the polarization of EtOH molecules, leading to the formation of adsorbed CH_3 $-CH_2\cdot$ and H· species. Subsequently, the CH_3 $-CH_2\cdot$ species undergo catalysis and break down to generate methyl groups and serve as in situ sources of hydrogen, stimulating the conversion of lower alkylphenols into higher alkylphenols [33]. On the contrary, the selectivity toward higher alkylphenols was decreased when using 7Mo-20Ni/Ce. Meanwhile, coke measurement showed a decent trend in the order of 3%Mo (0.96%), 5%Mo (0.45%), and 7%Mo (0.40%), highlighting the significant functionality of Mo for impeding coke deposition owing to enhanced oxygen vacancies of catalyst.

The obtained results could be explained based on the distinct functions of Ni and Mo in the guaiacol HDO. Indeed, Ni was applied to boost EtOH dehydrogenation, dissociation of H_2 into hydrogen radicals, and deoxygenation reactions, while Mo's role focused on enhancing Ni particle dispersion, reducing particle size, and increasing oxygen vacancies in the catalyst. Therefore, it can be concluded that raising the Mo percentage from 3% to 5%, which coexisted with 20% Ni, favorably promoted the Ni active sites reactivity by improving dispersion and reducing Ni particle sizes along with providing sufficient oxygen vacancies over the catalyst. However, loading 7% Mo decreased the catalytic activity and selectivity likely due to lowering the ratio of Ni-to-Mo active sites.

3.3.5. Effect of different reaction temperatures

To evaluate the influence of various reaction temperatures on the product distribution of guaiacol HDO, the potential of 5Mo-20Ni/Ce, as the best catalyst, was primarily investigated for the H_2 production from supercritical EtOH at different temperatures (i.e., 280, 300, 320, and 340 °C). The relative content of produced H_2 (mol × 100) showed a sharp increasing trend from 0.77 at 280 °C to 5.49, 8.13, and 13.32 at 300, 320, and 340 °C, respectively. This phenomenon is attributed to the endothermic nature of EtOH dehydrogenation to acetaldehyde and the subsequent conversion of acetaldehyde to gaseous products (e.g., H_2) [56]. Consistent with this study, Lee et al. [18] reported the enhanced H_2 generation and accelerated EtOH dehydrogenation by increasing temperature from 275 to 350 °C using Ni/AC, Ni-Mo/AC, and Mg-Ni-Mo/AC catalysts.

To test the effect of the reaction temperature on the catalytic performance of 5Mo-20Ni/Ce for the deoxygenation and generation of phenol and alkylphenols, the HDO of guaiacol was also performed at different temperatures. The guaiacol conversion was considerably enhanced by increasing temperature, reaching a maximum (95.6%) at 340 °C (Table 3). Moreover, as shown in Fig. 11c, the content of 1-oxy compounds was greatly enhanced by growing temperature, reaching a maximum (93.6%) at 340 °C. In contrast, the proportion of 2-oxy compounds showed an opposite trend, decreasing from 79.7% to 6.4% by increasing the temperature from 280 to 340 °C. These findings reveal the effective removal of oxygen during the HDO of guaiacol at elevated temperatures, which is consistent with the findings of Gutierrez et al. [78].

According to Table 3, the selectivity of phenol was significantly influenced by increasing temperature, where its value augmented from approximately 0% at 280 °C to 7.8%, 9.2%, and 27.4% at 300, 320, and 340 °C, respectively. Moreover, the content of generated alkylphenols exhibited an increasing trend with increasing temperature, varying in the range of 16.1% to 66.0%. In particular, lower alkylphenols (C7-C10) such as 3-methylphenol (m-cresol), 2-ethylphenol, and 2-ethyl-5-methylphenol were the main compounds generated at a reaction temperature of 340 °C. Conversely, the proportions of Alk-methoxyphenols and methoxybenzenes decreased with increasing temperature. Similarly, Ma et al. [62] reported that guaiacol conversion over activated carbon-supported molybdenum carbide catalyst increased by increasing the temperature from 280 to 340 °C, reaching a maximum of 87%. Furthermore, the same study reported that selectivity toward the total phenolic compounds increased from 63% to 85%. Yan et al. [74] also reported increased guaiacol conversion from 53.3% to 96.5% with enhancing temperature from 280 to 320 °C and increased selectivities of phenol and alkylphenols.

The product distribution in the HDO of guaiacol is a function of temperature because of the temperature dependence of the activation energies for various possible reaction pathways in the HDO process [10]. In particular, the enhancement of phenol and alkylphenols at the expense of Alk-methoxyphenols and methoxybenzenes is primarily ascribed to the intensified deoxygenation and ring alkylation reactions [44], which exert a kinetic-improving influence as well as a thermodynamic inhibitory effect at high temperatures [79]. Remón et al. [79] found that the increase in 1-oxy compounds at the expense of 2-oxy compounds upon increasing the temperature in the catalytic HDO of guaiacol was attributed to the role of high temperatures in alleviating thermodynamic and kinetic limitations. Furthermore, the enhanced H_2 production and dissociation over the metallic Ni active sites and promoted EtOH cracking over the Ov sites of the catalyst at elevated temperatures, resulting in the supplementation of hydrogen radicals (H·) and alkyl groups in the HDO reactions, would be other reasons.
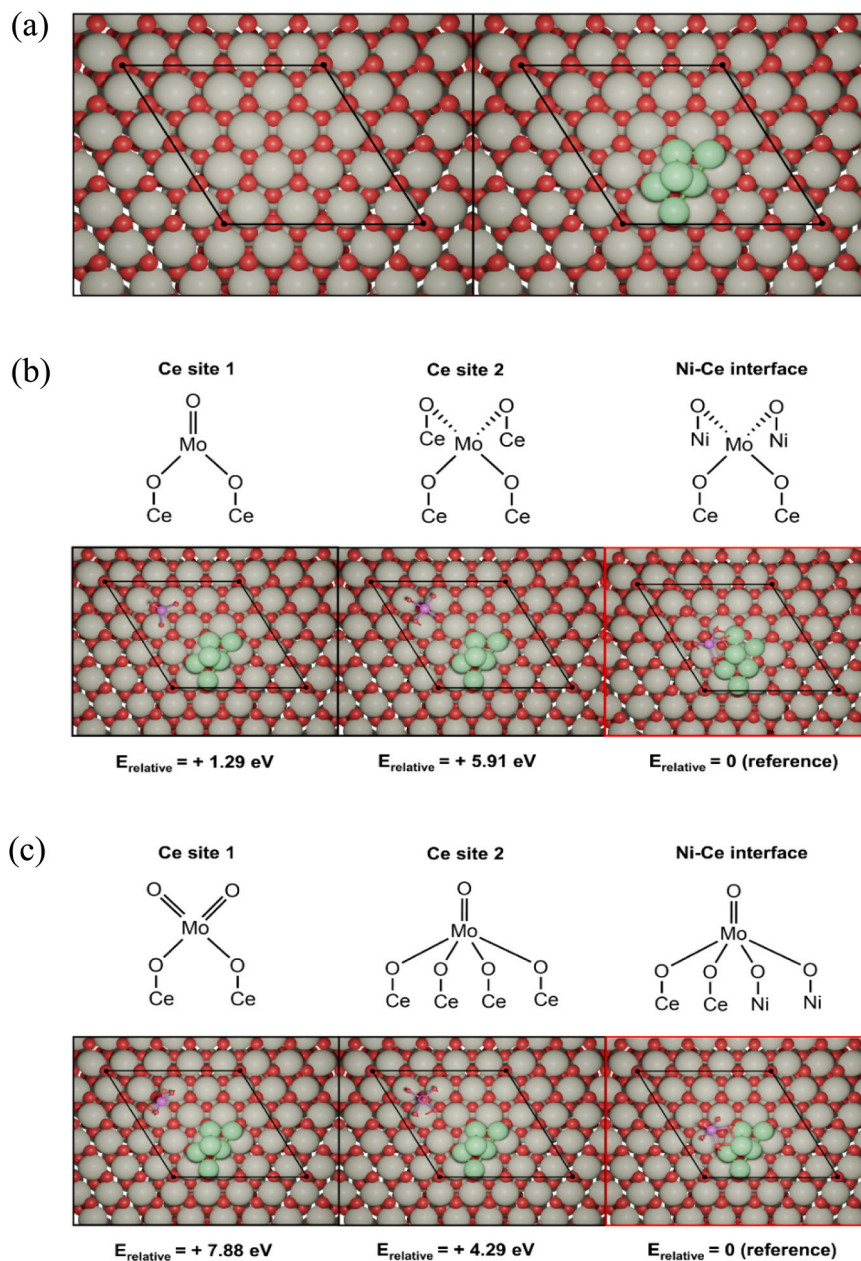

Fig. 12. Geometry-optimized surface models of $CeO_2(111)$ and $Ni/CeO_2(111)$ (a), and proposed structures of molybdena clusters with relative adsorption energies: (b) $Mo^{(IV)}$-Ni/Ce and (c) $Mo^{(VI)}$-Ni/Ce.

Therefore, temperature enhancement can simultaneously promote the HDO reaction rate and catalytic activity [80].

3.4. Theoretical analysis for the formation of oxygen vacancies in 20Ni/Ce and 5Mo-20Ni/Ce

3.4.1. Modeling of 20Ni/Ce and 5Mo-20Ni/Ce structures

Having confirmed that 5Mo-20Ni/Ce has superior catalytic performance due to its oxygen mobility property compared with 20Ni/Ce, the DFT calculations were further employed to identify the favorable site for oxygen vacancy and the catalysts' ability to form an oxygen vacancy. The surface model of CeO_2 was constructed with double layers of (111) plane of 4×4 supercell, and 15 Å of vacuum layer was introduced along the perpendicular direction to the surfaces to avoid the vertical interaction of periodic images. For the 20Ni/Ce catalyst model, the Ni_6 cluster was introduced and optimized over the $CeO_2(111)$ surface, giving the atom ratio of Ce to Ni at 5.33. (Fig. 12a). The Ni atoms that are directly contacted to the $CeO_2(111)$ surface have partially oxidized properties while a Ni atom that is placed on the uppermost top site of partially oxidized Ni atoms remains showing metallic properties [81]. Therefore, both metallic and partially oxidized Ni atoms are co-existing in this model. To construct the models of the 5Mo-20Ni/Ce catalyst, we considered both $Mo^{(VI)}$ and $Mo^{(IV)}$ oxide species and developed six different adsorption structures for molybdena clusters on $Ni/CeO_2(111)$ (Fig. 12b,c) [82,83]. The adsorption of molybdena clusters on the 20Ni/Ce interface exhibited the most stable adsorption energy compared to other structures, demonstrating that this adsorption site was thermodynamically the most favorable for the formation of molybdena clusters on $Ni/CeO_2(111)$ surface.

3.4.2. Oxygen vacancy formation energy calculations

Using DFT calculations, the energies required to create a single oxygen vacancy from the surfaces of $CeO_2(111)$, $Ni/CeO_2(111)$, $Mo^{(IV)}$-Ni/$CeO_2(111)$, and $Mo^{(VI)}$-Ni/$CeO_2(111)$ were calculated to identify the most stable site for oxygen vacancy formation and to assess the ease of forming the oxygen vacancy of each catalyst. For $Ni/CeO_2(111)$, $Mo^{(IV)}$-$Ni/CeO_2(111)$, and $Mo^{(VI)}$-$Ni/CeO_2(111)$ catalysts, the oxygen vacancy formation energies were calculated at three different oxygen sites as shown in Fig. 13a. The oxygen vacancy formation energy at O_v site 1 of $CeO_2(111)$ and $Ni/CeO_2(111)$ were calculated to be + 2.46 eV and + 2.73 eV, respectively. This indicated that the adsorption of the Ni cluster slightly increased the oxygen vacancy formation energy. However, upon adsorption of molybdena clusters on the surface, the oxygen vacancy formation energies were significantly reduced. For $Mo^{(IV)}$-$Ni/CeO_2(111)$ and $Mo^{(VI)}$-$Ni/CeO_2(111)$, oxygen vacancy formation energies at O_v site 1 (Mo-Ni-Ce interface) exhibit lower values compared to O_v site 2 (Ce site), and O_v site 3 (Ni site) (Fig. 13b). The calculated oxygen vacancy formation energies of $Mo^{(IV)}$-$Ni/CeO_2(111)$ and $Mo^{(VI)}$-$Ni/CeO_2(111)$ at O_v site 1 are + 1.18 eV and + 1.69 eV, respectively, while the energies for O_v site 2 are + 2.05 and + 2.23 eV, respectively. When compared to $CeO_2(111)$ and $Ni/CeO_2(111)$, both $Mo^{(IV)}$-Ni/CeO_2 (111) and $Mo^{(VI)}$-Ni/CeO_2 (111) show lower oxygen vacancy formation energies, regardless of the oxygen sites. Therefore, the presence of a molybdena cluster improves the formation of oxygen vacancies, leading to a more thermodynamically favorable formation of oxygen vacancies.

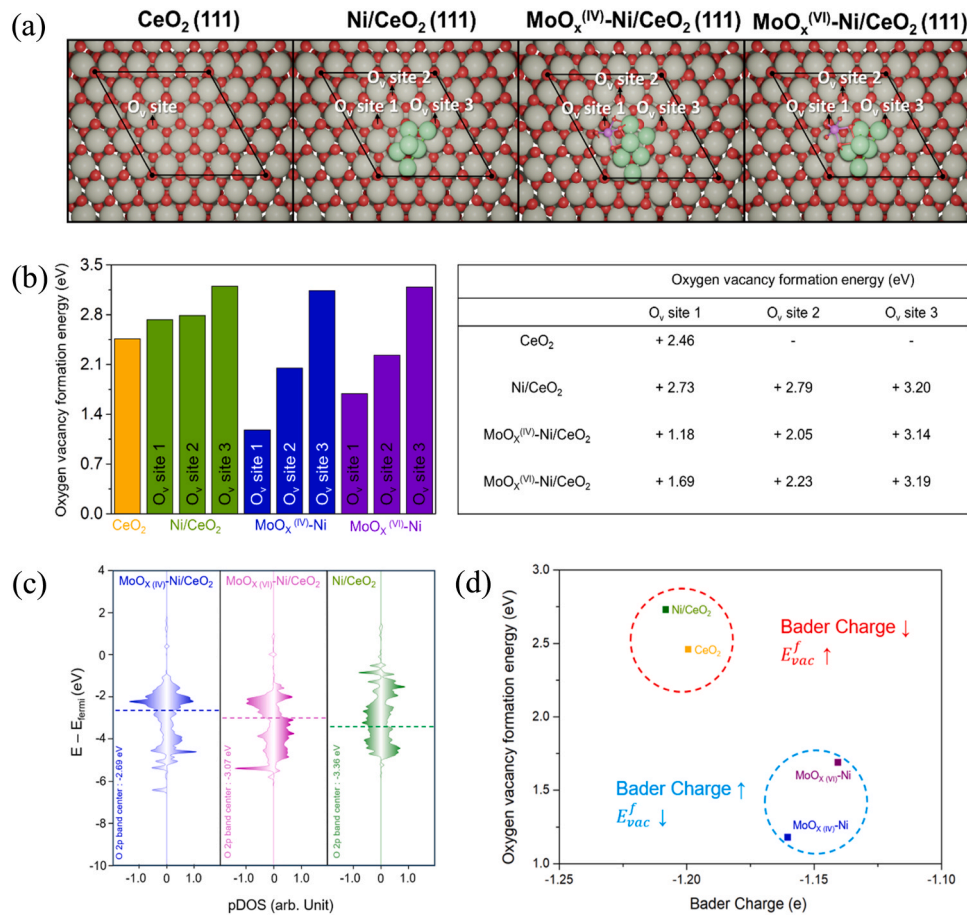The same conclusion could also be reached through the calculation

Fig. 13. (a) Oxygen vacancy formation sites of $CeO_2(111)$, $Ni/CeO_2(111)$, $Mo^{(IV)}$-Ni/Ce, and $Mo^{(VI)}$-Ni/Ce, (b) The calculated oxygen vacancy formation energies at each oxygen site, (c) The partial density of state (pDOS) of oxygen p band of structures of $Ni/CeO_2(111)$, $Mo^{(IV)}$-Ni/Ce and, $Mo^{(VI)}$-Ni/Ce, and (d) Bader charge analysis at the O_v site 1.

	Oxygen vacancy formation energy (eV)		
	O_v site 1	O_v site 2	O_v site 3
CeO_2	+ 2.46	-	-
Ni/CeO_2	+ 2.73	+ 2.79	+ 3.20
$MoO_x^{(IV)}$-Ni/CeO_2	+ 1.18	+ 2.05	+ 3.14
$MoO_x^{(VI)}$-Ni/CeO_2	+ 1.69	+ 2.23	+ 3.19

of the density of states (DOS) and Bader charge. The DOS calculation can identify the location of the O 2p band center, which can serve as a descriptor for determining the oxygen vacancy formation energy. The systems with a higher O 2p band center towards the Fermi level are more likely to form oxygen holes, hence lowering the oxygen vacancy formation energy [84]. According to the DOS calculations, the presence of a molybdena cluster on $Ni/CeO_2(111)$ leads to an upshift of the O 2p band center of the oxygen site near the Mo-Ni-Ce interface (Fig. 13c). This result was consistent with the decrease in oxygen vacancy formation energy when molybdena clusters were introduced on $Ni/CeO_2(111)$. In addition, Bader charge analysis was further conducted to reveal the correlation between the accumulated charges on oxygen sites to the oxygen vacancy formation energy (Fig. 13d). The adsorption of the molybdena cluster on $Ni/CeO_2(111)$ decreases the charge on the oxygen site. By comparing the oxygen vacancy formation energy with the Bader charge at the oxygen site near the Mo-Ni-Ce interface, the oxygen site with a lower Bader charge shows less oxygen vacancy formation energy. This is likely attributed to the lower amount of excited charge. Since the smaller amount of charge is excited when the oxygen site has a lower Bader charge, less energy is required to remove an oxygen atom from the surface [85,86].

4. Conclusion

The catalytic HDO of guaiacol in supercritical EtOH was conducted using 20Ni/Ce and 5Mo-20Ni/Ce catalysts for the selective generation of phenol and alkylphenols without the addition of external H_2. The addition of 5% Mo as a promoter to 20% Ni/Ce considerably enhanced H_2 generation from EtOH cracking. In guaiacol's HDO, higher conversion and increased deoxygenation were achieved by employing 5Mo-20Ni/Ce compared with 20Ni/Ce. The selectivities of phenol and alkylphenols were obtained at 20.6% and 9.9%, respectively, using 20Ni/Ce, and 7.8% and 29.0% using 5Mo-20Ni/Ce. The superior performance of 5Mo-20Ni/Ce was ascribed to the intensified EtOH dehydrogenation, hydrogen radicals supplement, and the acceleration of the HDO reactions due to the promoted Ni dispersion and oxygen mobility properties of the catalyst. Testing 5Mo-20Ni/Ce in three consecutive cycles revealed the maintenance of catalyst efficiency for stimulating the EtOH cracking, supplementing hydrogen radicals, and HDO reactions. The examination of different Ni and Mo loading amounts revealed that the most effective catalyst performance occurs via a coexistence of 20% Ni and 5% Mo (5Mo-20Ni/Ce). Using 5Mo-20Ni/Ce, higher temperatures significantly boosted guaiacol conversion and selectivities for phenol and alkylphenols, achieving 95.6%, 27.4%, and 66.0%, respectively, at 340 °C. This was attributed to reduced kinetic and thermodynamic constraints in guaiacol's HDO reactions. Catechol has been suggested to be the main intermediate formed via guaiacol demethylation, followed by transformation into phenol and alkylphenols through a series of deoxygenation and alkylation reactions. The study employed DFT calculations to analyze the oxygen vacancy formation energies on various catalyst surfaces, revealing that the introduction of molybdena clusters significantly reduced the energy needed for oxygen vacancy formation, particularly at the Mo-Ni-Ce interface. This highlights improved catalytic abilities for generating oxygen vacancies within the 5Mo-20Ni/Ce catalyst. Overall, the catalytic HDO of guaiacol in supercritical EtOH using catalysts with highly dispersed Ni active sites and high oxygen transfer potential without the supplement of external H_2 would be a promising option for upgrading bio-oil and generating value-added phenol and alkylphenols.

CRediT authorship contribution statement

Park Young-Kwon: Conceptualization, Project administration, Resources, Supervision, Writing – review & editing. **Ko Chang Hyun:** Writing – review & editing. **Han Jeong Woo:** Supervision, Writing – review & editing. **Kang Bo Sung:** Data curation, Formal analysis,

Investigation, Writing – original draft. **Hwang Jinwoo:** Investigation, Writing – original draft. **Jae Jungho:** Writing – review & editing. **Valizadeh Soheil:** Data curation, Formal analysis, Investigation, Writing – original draft. **Khani Yasin:** Data curation, Formal analysis, Investigation, Writing – original draft.

Declaration of Competing Interest

The authors declare that they have no known competing financial interests or personal relationships that could have appeared to influence the work reported in this paper.

Data Availability

The authors do not have permission to share data.

Appendix A. Supporting information

Supplementary data associated with this article can be found in the online version at doi:10.1016/j.apcatb.2024.123823.

References

[1] Z. Cai, J. Long, Y. Li, L. Ye, B. Yin, L.J. France, J. Dong, L. Zheng, H. He, S. Liu, Selective production of diethyl maleate via oxidative cleavage of lignin aromatic unit, Chem 5 (9) (2019) 2365–2377.

[2] C. Li, X. Zhao, A. Wang, G.W. Huber, T. Zhang, Catalytic transformation of lignin for the production of chemicals and fuels, Chem. Rev. 115 (21) (2015) 11559–11624.

[3] S.S. Wong, R. Shu, J. Zhang, H. Liu, N. Yan, Downstream processing of lignin derived feedstock into end products, Chem. Soc. Rev. 49 (15) (2020) 5510–5560.

[4] H. Choi, Y.T. Kim, Y.F. Tsang, J. Lee, Integration of thermochemical conversion processes for waste-to-energy: A review, Korean J. Chem. Eng. 40 (2023) 1815–1821.

[5] W. Zhang, Z. Wang, T. Ge, C. Yang, W. Song, S. Li, R. Ma, Catalytic pyrolysis of corn straw for deoxygenation of bio-oil with different types of catalysts, Korean J. Chem. Eng. 39 (2022) 1240–1247.

[6] Y. Elkasabi, C.A. Mullen, A.L. Pighinelli, A.A. Boateng, Hydrodeoxygenation of fast-pyrolysis bio-oils from various feedstocks using carbon-supported catalysts, Fuel Process. Technol. 123 (2014) 11–18.

[7] Z. Cai, F. Wang, X. Zhang, R. Ahishakiye, Y. Xie, Y. Shen, Selective hydrodeoxygenation of guaiacol to phenolics over activated carbon supported molybdenum catalysts, Mol. Catal. 441 (2017) 28–34.

[8] H. Ma, W. Zhang, D. Chen, Catalytic hydrodeoxygenation of phenolic compounds over Ru-MoFeP/Al$_2$O$_3$ catalyst, Catal. Today 408 (2023) 50–57.

[9] R.D. Patil, Y. Sasson, Selective transfer hydrogenation of phenol to cyclohexanone on supported palladium catalyst using potassium formate as hydrogen source under open atmosphere, Appl. Catal. A: Gen. 499 (2015) 227–231.

[10] H. Shafaghat, P.S. Rezaei, W.M.A.W. Daud, Effective parameters on selective catalytic hydrodeoxygenation of phenolic compounds of pyrolysis bio-oil to high-value hydrocarbons, RSC Adv. 5 (126) (2015) 103999–104042.

[11] E. Roldugina, E. Naranov, A. Maximov, E. Karakhanov, Hydrodeoxygenation of guaiacol as a model compound of bio-oil in methanol over mesoporous noble metal catalysts, Appl. Catal. 553 (2018) 24–35.

[12] C. Li, J. Shi, K. Zhang, Y. Wang, Z. Tang, M. Chen, Efficient conversion of Kraft lignin to guaiacol and 4-alkyl guaiacols over Fe-Fe$_3$C/C based catalyst under supercritical ethanol, Fuel 315 (2022) 123249.

[13] D. Laurenti, P. Afanasiev, C. Geantet, Hydrodeoxygenation of guaiacol with CoMo catalysts. Part I: promoting effect of cobalt on HDO selectivity and activity, Appl. Catal. B: Environ. 101 (3-4) (2011) 239–245.

[14] R.C. Runnebaum, T. Nimmanwudipong, D.E. Block, B.C. Gates, Catalytic conversion of compounds representative of lignin-derived bio-oils: a reaction network for guaiacol, anisole, 4-methylanisole, and cyclohexanone conversion catalysed by Pt/γ-Al$_2$O$_3$, Catal. Sci. Technol. 2 (1) (2012) 113–118.

[15] X. Huang, T.I. Korányi, M.D. Boot, E.J. Hensen, Catalytic depolymerization of lignin in supercritical ethanol, ChemSusChem 7 (8) (2014) 2276–2288.

[16] I.B. Adilina, N. Rinaldi, S.P. Simanungkalit, F. Aulia, F. Oemry, G.B. Stenning, I. P. Silverwood, S.F. Parker, Hydrodeoxygenation of guaiacol as a bio-oil model

compound over pillared clay-supported nickel–molybdenum catalysts, J. Phys. Chem. C. 123 (35) (2019) 21429–21439.

[17] M. Saidi, F. Samimi, D. Karimipourfard, T. Nimmanwudipong, B.C. Gates, M. R. Rahimpour, Upgrading of lignin-derived bio-oils by catalytic hydrodeoxygenation, Energy Environ. Sci. 7 (1) (2014) 103–129.

[18] J.-H. Lee, I.-G. Lee, W. Jeon, J.-H. Ha, K.-Y. Lee, Catalytic upgrading of bio-tar over a MgNiMo/activated charcoal catalyst under supercritical ethanol conditions, Catal. Today 316 (2018) 237–243.

[19] S. Beyhan, J.-M. Léger, F. Kadırgan, Understanding the influence of Ni, Co, Rh and Pd addition to PtSn/C catalyst for the oxidation of ethanol by in situ Fourier transform infrared spectroscopy, Appl. Catal. B: Environ. 144 (2014) 66–74.

[20] M. Chen, J. Shi, Y. Wang, Z. Tang, Z. Yang, J. Wang, H. Zhang, Conversion of Kraft lignin to phenol monomers and liquid fuel over trimetallic catalyst W-Ni-Mo/ sepiolite under supercritical ethanol, Fuel 303 (2021) 121332.

[21] M. Oregui-Bengoechea, I. Gandarias, N. Miletić, S.F. Simonsen, A. Kronstad, P. L. Arias, T. Barth, Thermocatalytic conversion of lignin in an ethanol/formic acid medium with NiMo catalysts: Role of the metal and acid sites, Appl. Catal. B: Environ. 217 (2017) 353–364.

[22] M. Bykova, D.Y. Ermakov, V. Kaichev, O. Bulavchenko, A. Saraev, M.Y. Lebedev, V. Yakovlev, Ni-based sol–gel catalysts as promising systems for crude bio-oil upgrading: guaiacol hydrodeoxygenation study, Appl. Catal. B: Environ. 113 (2012) 296–307.

[23] B. Yoosuk, D. Tumnantong, P. Prasassarakich, Amorphous unsupported Ni–Mo sulfide prepared by one step hydrothermal method for phenol hydrodeoxygenation, Fuel 91 (1) (2012) 246–252.

[24] A. Zuliani, O. Kikhtyanin, C.M. Cova, D. Rodriguez-Padron, D. Kubička, R. Luque, Boosting the Ni-catalyzed hydrodeoxygenation (HDO) of anisole using scrap catalytic converters, Adv. Sustain. Syst. 6 (4) (2022) 2100394.

[25] M. Chen, Z. Tang, Y. Wang, J. Shi, C. Li, Z. Yang, J. Wang, Catalytic depolymerization of Kraft lignin to liquid fuels and guaiacol over phosphorus modified Mo/Sepiolite catalyst, Chem. Eng. J. 427 (2022) 131761.

[26] H. Shafaghat, Y.F. Tsang, J.-K. Jeon, J.M. Kim, Y. Kim, S. Kim, Y.-K. Park, In-situ hydrogenation of bio-oil/bio-oil phenolic compounds with secondary alcohols over a synthesized mesoporous Ni/CeO₂ catalyst, Chem. Eng. J. 382 (2020) 122912.

[27] T. Prasomsri, T. Nimmanwudipong, Y. Román-Leshkov, Effective hydrodeoxygenation of biomass-derived oxygenates into unsaturated hydrocarbons by MoO₃ using low H₂ pressures, Energy Environ. Sci. 6 (6) (2013) 1732–1738.

[28] V. Mortola, S. Damyanova, D. Zanchet, J. Bueno, Surface and structural features of Pt/CeO₂-La₂O₃-Al₂O₃ catalysts for partial oxidation and steam reforming of methane, Appl. Catal. B: Environ. (2011) 221–236.

[29] S.M. Schimming, O.D. LaMont, M. König, A.K. Rogers, A.D. D'Amico, M.M. Yung, C. Sievers, Hydrodeoxygenation of guaiacol over ceria–zirconia catalysts, ChemSusChem 8 (12) (2015) 2073–2083.

[30] A. Piras, A. Trovarelli, G. Dolcetti, Remarkable stabilization of transition alumina operated by ceria under reducing and redox conditions, Appl. Catal. B: Environ. 28 (2) (2000) L77–L81.

[31] M. Chen, H. Li, Y. Wang, Z. Tang, W. Dai, C. Li, Z. Yang, J. Wang, Lignin depolymerization for aromatic compounds over Ni-Ce/biochar catalyst under aqueous-phase glycerol, Appl. Energy 332 (2023) 120489.

[32] Y. Du, C. Qin, Y. Xu, D. Xu, J. Bai, G. Ma, M. Ding, Ni nanoparticles dispersed on oxygen vacancies-rich CeO₂ nanoplates for enhanced low-temperature CO₂ methanation performance, Chem. Eng. J. 418 (2021) 129402.

[33] Z. Tang, Y. Wang, M. Chen, H. Li, L. Li, Z. Zhou, C. Li, Z. Yang, J. Wang, Lignin catalytic depolymerization for phenolic monomers: boosting the selective cleavage of β-O-4 bonds of lignin by Mo= O and Al (IV)–O–BO₂ interfacial sites in B–Mo/ sepiolite, ACS Sustain. Chem. 11 (47) (2023) 16722–16738.

[34] K. Cui, L. Yang, Z. Ma, F. Yan, K. Wu, Y. Sang, H. Chen, Y. Li, Selective conversion of guaiacol to substituted alkylphenols in supercritical ethanol over MoO₃, Appl. Catal. B: Environ. 219 (2017) 592–602.

[35] S. Natesakhawat, R.B. Watson, X. Wang, U.S. Ozkan, Deactivation characteristics of lanthanide-promoted sol–gel Ni/Al₂O₃ catalysts in propane steam reforming, J. Catal. 234 (2) (2005) 496–508.

[36] M. Chen, W. Dai, Y. Wang, Z. Tang, H. Li, C. Li, Z. Yang, J. Wang, Selective catalytic depolymerization of lignin to guaiacols over Mo-Mn/sepiolite in supercritical ethanol, Fuel 333 (2023) 126365.

[37] W. Jin, L. Pastor-Pérez, J.J. Villora-Picó, A. Sepúlveda-Escribano, S. Gu, T. Reina, Investigating new routes for biomass upgrading:"H₂-free" hydrodeoxygenation using Ni-based catalysts, ACS Sustain. Chem. Eng. 7 (19) (2019) 16041–16049.

[38] G. Kresse, J. Furthmüller, Efficient iterative schemes for ab initio total-energy calculations using a plane-wave basis set, Phys. Rev. B 54 (16) (1996) 11169.

[39] D.S. Sholl, J.A. Steckel, Density Functional Theory: A Practical Introduction, John Wiley & Sons, 2022.

[40] S. Fernandez, M.L. Ostraat, J.A. Lawrence III, K. Zhang, Tailoring the hierarchical architecture of beta zeolites using base leaching and pore-directing agents, Microporous Mesoporous Mater. 263 (2018) 201–209.

[41] M. Hussain, D. Fino, N. Russo, N₂O decomposition by mesoporous silica supported Rh catalysts, J. Hazard. Mater. 211 (2012) 255–265.

[42] R.R. Barton, M. Carrier, C. Segura, J.L.G. Fierro, N. Escalona, S.W. Peretti, Ni/ HZSM-5 catalyst preparation by deposition-precipitation. Part 1. Effect of nickel loading and preparation conditions on catalyst properties, Appl. Catal. A: Gen. 540 (2017) 7–20.

[43] Q.-H. Xia, S.-C. Shen, J. Song, S. Kawi, K. Hidajat, Structure, morphology, and catalytic activity of β zeolite synthesized in a fluoride medium for asymmetric hydrogenation, J. Catal. 219 (1) (2003) 74–84.

[44] J.-H. Lee, I.-G. Lee, J.-Y. Park, K.-Y. Lee, Efficient upgrading of pyrolysis bio-oil over Ni-based catalysts in supercritical ethanol, Fuel 241 (2019) 207–217.

[45] V. Vinila, J. Isac, Synthesis and structural studies of superconducting perovskite GdBa₂Ca₃Cu₄O₁₀.₅₊δ nanosystems. Design, Fabrication, and Characterization of Multifunctional Nanomaterials, Elsevier, 2022, pp. 319–341.

[46] M.M. Natile, A. Glisenti, Nanostructured CeO₂ powders by XPS, Surf. Sci. Spectra 13 (1) (2006) 17–30.

[47] H. Li, F. Meng, J. Gong, Z. Fan, R. Qin, Structural, morphological and optical properties of shuttle-like CeO₂ synthesized by a facile hydrothermal method, J. Alloy. Compd. 722 (2017) 489–498.

[48] A.M. Hengne, A.K. Samal, L.R. Enakonda, M. Harb, L.E. Gevers, D.H. Anjum, M. N. Hedhili, Y. Saih, K.-W. Huang, J.-M. Basset, Ni-Sn-supported ZrO₂ catalysts modified by indium for selective CO₂ hydrogenation to methanol, ACS Omega 3 (4) (2018) 3688–3701.

[49] S. Jain, J. Shah, N.S. Negi, C. Sharma, R.K. Kotnala, Significance of interface barrier at electrode of hematite hydroelectric cell for generating ecopower by water splitting, Int. J. Energy Res. 43 (9) (2019) 4743–4755.

[50] C. Wu, D. Liu, H. Li, J. Li, Molybdenum carbide-decorated metallic cobalt@ nitrogen-doped carbon polyhedrons for enhanced electrocatalytic hydrogen evolution, Small 14 (16) (2018) 1704227.

[51] J. Lu, X. Zhang, J.J. Bravo-Suárez, T. Fujitani, S.T. Oyama, Effect of composition and promoters in Au/TS-1 catalysts for direct propylene epoxidation using H₂ and O₂, Catal. Today 147 (3-4) (2009) 186–195.

[52] D. Wang, Z. Liu, Q. Liu, Synthesis of 1-Butanol from Ethanol over Calcium Ethoxide: Experimental and Density Functional Theory Simulation, J. Phys. Chem. C. 123 (37) (2019) 22932–22940.

[53] J. Ob-eye, P. Praserthdam, B. Jongsomjit, Dehydrogenation of ethanol to acetaldehyde over different metals supported on carbon catalysts, Catalysts 9 (1) (2019) 66.

[54] H. Wang, G. Miao, L. Kong, H. Luo, Y. Zhang, X. Zhao, S. Li, Y. Sun, Efficient one-pot valorization of ethanol to 1-butanol over an earth-abundant Ni–MgO catalyst under mild conditions, Sustain. Energy Fuels 4 (4) (2020) 1612–1615.

[55] J. Scalbert, F. Thibault-Starzyk, R. Jacquot, D. Morvan, F. Meunier, Ethanol condensation to butanol at high temperatures over a basic heterogeneous catalyst: How relevant is acetaldehyde self-aldolization? J. Catal. 311 (2014) 28–32.

[56] D. Gao, Y. Feng, H. Yin, A. Wang, T. Jiang, Coupling reaction between ethanol dehydrogenation and maleic anhydride hydrogenation catalyzed by Cu/Al₂O₃, Cu/ ZrO₂, and Cu/ZnO catalysts, Chem. Eng. J. 233 (2013) 349–359.

[57] A. Kumar, Ethanol decomposition and dehydrogenation for hydrogen production: a review of heterogeneous catalysts, Ind. Eng. Chem. Res. 60 (46) (2021) 16561–16576.

[58] T.S. Khan, F. Jalid, M.A. Haider, First-principle microkinetic modeling of ethanol dehydrogenation on metal catalyst surfaces in non-oxidative environment: design of bimetallic alloys, Top. Catal. 61 (2018) 1820–1831.

[59] V. Palma, C. Ruocco, M. Cortese, M. Martino, Bioalcohol reforming: an overview of the recent advances for the enhancement of catalyst stability, Catalysts 10 (6) (2020) 665.

[60] A. Sato, D. Volanti, D. Meira, S. Damyanova, E. Longo, J. Bueno, Effect of the ZrO₂ phase on the structure and behavior of supported Cu catalysts for ethanol conversion, J. Catal. 307 (2013) 1–17.

[61] S. Chen, C. Pei, J. Gong, Insights into interface engineering in steam reforming reactions for hydrogen production, Energy Environ. Sci. 12 (12) (2019) 3473–3495.

[62] R. Ma, K. Cui, L. Yang, X. Ma, Y. Li, Selective catalytic conversion of guaiacol to phenols over a molybdenum carbide catalyst, Chem. Commun. 51 (51) (2015) 10299–10301.

[63] S.-K. Wu, P.-C. Lai, Y.-C. Lin, H.-P. Wan, H.-T. Lee, Y.-H. Chang, Atmospheric hydrodeoxygenation of guaiacol over alumina-, zirconia-, and silica-supported nickel phosphide catalysts, ACS Sustain. Chem. 1 (3) (2013) 349–358.

[64] M. Bykova, D.Y. Ermakov, S. Khromova, A. Smirnov, M.Y. Lebedev, V. Yakovlev, Stabilized Ni-based catalysts for bio-oil hydrotreatment: Reactivity studies using guaiacol, Catal. Today 220 (2014) 21–31.

[65] H.W. Lee, B.R. Jun, H. Kim, D.H. Kim, J.-K. Jeon, S.H. Park, C.H. Ko, T.-W. Kim, Y.- K. Park, Catalytic hydrodeoxygenation of 2-methoxy phenol and dibenzofuran over Pt/mesoporous zeolites, Energy 81 (2015) 33–40.

[66] M. Zhou, Y. Wang, Y. Wang, G. Xiao, Catalytic conversion of guaiacol to alcohols for bio-oil upgrading, J. Energy Chem. 24 (4) (2015) 425–431.

[67] C. García-Mendoza, C. Santolalla-Vargas, L.G. Woolfolk, P. del Angel, J. De los Reyes, Effect of TiO₂ in supported NiWS catalysts for the hydrodeoxygenation of guaiacol, Catal. Today 377 (2021) 145–156.

[68] H. Lee, H. Kim, M.J. Yu, C.H. Ko, J.-K. Jeon, J. Jae, S.H. Park, S.-C. Jung, Y.- K. Park, Catalytic hydrodeoxygenation of bio-oil model compounds over Pt/HY catalyst, Sci. Rep. 6 (1) (2016) 28765.

[69] C. Loricera, B. Pawelec, A. Infantes-Molina, M. Álvarez-Galván, R. Huirache-Acuña, R. Nava, J. Fierro, Hydrogenolysis of anisole over mesoporous sulfided CoMoW/ SBA-15 (16) catalysts, Catal. Today 172 (1) (2011) 103–110.

[70] L. Yang, K. Seshan, Y. Li, Transetherification of guaiacol to o-ethoxyphenol with gamma Al₂O₃ as a catalyst in supercritical ethanol, Catal. Commun. 30 (2013) 36–39.

[71] D. Raikwar, S. Majumdar, D. Shee, Synergistic effect of Ni-Co alloying on hydrodeoxygenation of guaiacol over Ni-Co/Al₂O₃ catalysts, Mol. Catal. 499 (2021) 111290.

[72] X. Lan, E.J. Hensen, T. Weber, Hydrodeoxygenation of guaiacol over Ni₂P/ SiO₂–reaction mechanism and catalyst deactivation, Appl. Catal. A: Gen. 550 (2018) 57–66.

[73] F. Mai, K. Cui, Z. Wen, K. Wu, F. Yan, M. Chen, H. Chen, Y. Li, Highly selective conversion of guaiacol to tert-butylphenols in supercritical ethanol over a H$_2$WO$_4$ catalyst, RSC Adv. 9 (5) (2019) 2764–2771.

[74] F. Yan, Y. Sang, Y. Bai, K. Wu, K. Cui, Z. Wen, F. Mai, Z. Ma, L. Yu, H. Chen, Guaiacol demethoxylation catalyzed by Re$_2$O$_7$ in ethanol, Catal. Today 355 (2020) 231–237.

[75] W. Wang, Y. Yang, H. Luo, T. Hu, W. Liu, Amorphous Co–Mo–B catalyst with high activity for the hydrodeoxygenation of bio-oil, Catal. Commun. 12 (6) (2011) 436–440.

[76] Z. Luo, Z. Zheng, L. Li, Y.-T. Cui, C. Zhao, Bimetallic Ru–Ni catalyzed aqueous-phase guaiacol hydrogenolysis at low H$_2$ pressures, ACS Catal. 7 (12) (2017) 8304–8313.

[77] L. Xiang, G. Fan, L. Yang, L. Zheng, F. Li, Structure-tunable pompon-like RuCo catalysts: Insight into the roles of atomically dispersed Ru-Co sites and crystallographic structures for guaiacol hydrodeoxygenation, J. Catal. 398 (2021) 76–88.

[78] A. Gutierrez, R.K. Kaila, M.L. Honkela, R. Slioor, A.O.I. Krause, Hydrodeoxygenation of guaiacol on noble metal catalysts, Catal. Today 147 (3-4) (2009) 239–246.

[79] J. Remón, E. Ochoa, C. Foguet, J.L. Pinilla, I. Suelves, Towards a sustainable bio-fuels production from lignocellulosic bio-oils: Influence of operating conditions on the hydrodeoxygenation of guaiacol over a Mo$_2$C/CNF catalyst, Fuel Process. Technol. 191 (2019) 111–120.

[80] A.L. Jongerius, R.W. Gosselink, J. Dijkstra, J.H. Bitter, P.C. Bruijnincx, B. M. Weckhuysen, Carbon nanofiber supported transition-metal carbide catalysts for the hydrodeoxygenation of guaiacol, ChemCatChem 5 (10) (2013) 2964–2972.

[81] Z. Mao, P.G. Lustemberg, J.R. Rumptz, M.V. Ganduglia-Pirovano, C.T. Campbell, Ni nanoparticles on CeO$_2$ (111): energetics, electron transfer, and structure by Ni adsorption calorimetry, spectroscopies, and density functional theory, ACS Catal. 10 (9) (2020) 5101–5114.

[82] K. Kurleto, F. Tielens, J. Handzlik, Isolated molybdenum (VI) and tungsten (VI) oxide species on partly dehydroxylated silica: A computational perspective, J. Phys. Chem. C. 124 (5) (2020) 3002–3013.

[83] S. Chempath, A.T. Bell, A DFT study of the mechanism and kinetics of methane oxidation to formaldehyde occurring on silica-supported molybdena, J. Catal. 247 (1) (2007) 119–126.

[84] N. Yu, Z.-J. Zhang, Y.-M. Chai, B. Dong, Regulation engineering of the surface and structure of perovskite-based electrocatalysts for the oxygen evolution reaction, Mater. Chem. Front. 7 (19) (2023) 4236–4258.

[85] V. Fung, Z. Wu, D.-e Jiang, New bonding model of radical adsorbate on lattice oxygen of perovskites, J. Phys. Chem. Lett. 9 (21) (2018) 6321–6325.

[86] Y. Hinuma, S. Mine, T. Toyao, T. Kamachi, K.-i Shimizu, Factors determining surface oxygen vacancy formation energy in ternary spinel structure oxides with zinc, Phys. Chem. Chem. Phys. 23 (41) (2021) 23768–23777.